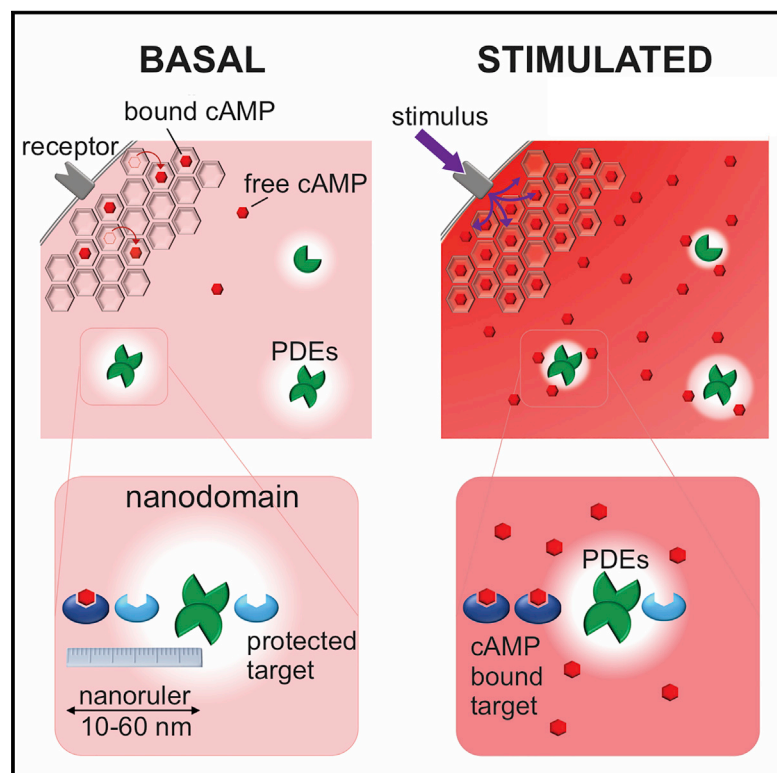


Optical Mapping of cAMP Signaling at the Nanometer Scale

Graphical Abstract



Authors

Andreas Bock, Paolo Annibale, Charlotte Konrad, ..., Sivaraj Sivaramakrishnan, Martin Falcke, Martin J. Lohse

Correspondence

andreas.bock@mdc-berlin.de (A.B.), m.lohse@mdc-berlin.de (M.J.L.)

In Brief

Mapping cAMP dynamics and concentrations in live cells reveals how maintaining low levels of free second messengers enables formation of nanometer-sized signaling compartments.

Highlights

- Under basal conditions, most cAMP in cells is bound and its free concentration is low
- Individual phosphodiesterases create nanometer-size domains of even lower cAMP
- In such nanodomains, cAMP targets are protected from cAMP signals
- Receptor stimuli increase cAMP to flood nanodomains and trigger downstream effects

Article

Optical Mapping of cAMP Signaling at the Nanometer Scale

Andreas Bock,^{1,2,7,*} Paolo Annibale,^{1,2,7} Charlotte Konrad,^{1,2} Annette Hannawacker,² Selma E. Anton,^{1,2} Isabella Maiellaro,² Ulrike Zabel,² Sivaraj Sivaramakrishnan,³ Martin Falcke,^{1,4} and Martin J. Lohse^{1,2,5,6,8,*}

¹Max Delbrück Center for Molecular Medicine in the Helmholtz Association, Robert-Rössle-Str. 10, 13125 Berlin, Germany

²Institute of Pharmacology and Toxicology, University of Würzburg, Versbacher Str. 9, 97078 Würzburg, Germany

³Department of Genetics, Cell Biology, and Development, University of Minnesota, Minneapolis, MN 55455, USA

⁴Department of Physics, Humboldt University, Newtonstr. 15, 12489 Berlin, Germany

⁵Institute for Chemistry and Biochemistry, Free University, Takustr. 3, 14195 Berlin, Germany

⁶SAR Bioscience Institute, 82152 Munich/Planegg, Germany

⁷These authors contributed equally

⁸Lead Contact

*Correspondence: andreas.bock@mdc-berlin.de (A.B.), m.lohse@mdc-berlin.de (M.J.L.)

<https://doi.org/10.1016/j.cell.2020.07.035>

SUMMARY

Cells relay a plethora of extracellular signals to specific cellular responses by using only a few second messengers, such as cAMP. To explain signaling specificity, cAMP-degrading phosphodiesterases (PDEs) have been suggested to confine cAMP to distinct cellular compartments. However, measured rates of fast cAMP diffusion and slow PDE activity render cAMP compartmentalization essentially impossible. Using fluorescence spectroscopy, we show that, contrary to earlier data, cAMP at physiological concentrations is predominantly bound to cAMP binding sites and, thus, immobile. Binding and unbinding results in largely reduced cAMP dynamics, which we term “buffered diffusion.” With a large fraction of cAMP being buffered, PDEs can create nanometer-size domains of low cAMP concentrations. Using FRET-cAMP nanorulers, we directly map cAMP gradients at the nanoscale around PDE molecules and the areas of resulting downstream activation of cAMP-dependent protein kinase (PKA). Our study reveals that spatiotemporal cAMP signaling is under precise control of nanometer-size domains shaped by PDEs that gate activation of downstream effectors.

INTRODUCTION

Hundreds of cell surface receptors, notably G protein-coupled receptors (GPCRs), signal via the second messenger cyclic adenosine monophosphate (cAMP) and its effector proteins, in particular protein kinase A (PKA). This pathway is central to key physiological functions and, hence, to many diseases, making it a highly attractive therapeutic target (Nikolaev et al., 2010; Gold et al., 2013; Zaccolo, 2009, 2011; Perera and Nikolaev, 2013). However, it is unclear how the huge number of receptors that change global cellular cAMP levels can result in specific cellular responses. To explain receptor-specific responses observed in experiments and how these responses might differ in different regions of a cell, many researchers have proposed cAMP compartmentalization (Brunton et al., 1979; Hayes et al., 1980; Buxton and Brunton, 1983). cAMP-degrading phosphodiesterases (PDEs) have been proposed to play a crucial role in establishing the cAMP gradients that are necessary to create such compartments (Houslay, 2010; Terrin et al., 2006; Mika et al., 2012; Stangherlin and Zaccolo, 2012).

However, several studies have determined that cAMP is highly diffusible in intact cells (Bacskai et al., 1993; Nikolaev et al.,

2004, 2006; Chen et al., 1999; Richards et al., 2016; Agarwal et al., 2016; Huang and Gillette, 1993; Table S1), and PDEs have low catalytic rates (Omori and Kotera, 2007; Conti and Beavo, 2007; Bender and Beavo, 2006). Therefore, cAMP should very rapidly equilibrate in a cell (Rich et al., 2000, 2001; Feinstein et al., 2012; Lohse et al., 2017; Xin et al., 2015), and this would prevent the existence of compartments with different concentrations of cAMP. Thus, the important question of whether and how intracellular cAMP might be compartmentalized has remained unresolved for decades.

We therefore set out to address this controversy by developing tools and methods to directly measure and characterize cAMP mobility in intact cells and at physiological levels and to measure cAMP levels and gradients in real time and with a spatial accuracy in the nanometer range.

RESULTS

cAMP Buffering Restricts cAMP Dynamics in Intact Cells

To visualize how signaling by cAMP is patterned, we aimed to develop and use new technologies that allow analysis of cAMP diffusion and possible cAMP gradients at the nanometer scale.

To assess intracellular cAMP diffusion under physiological conditions, we set out to directly measure cAMP dynamics in intact cells. We designed the cell-permeable fluorogenic cAMP analog 8-(2-(5(6)-carboxyfluoresceindiacetate)-aminoethylthio)adenosine-3',5'-cyclic monophosphate (8-FDA-cAMP), which becomes fluorescent when hydrolyzed to the corresponding fluorescein compound 8-F-cAMP by intracellular esterases (Figure 1A). A detailed characterization of this compound is given in [Methods S1](#), including optical properties, equivalence to cAMP in binding to and activation of PKA, as well as resistance to degradation by PDEs.

The diffusion properties of this compound were then analyzed in intact cells by applying techniques that can report a wide range of diffusion speeds. Using a fluorescence fluctuation spectroscopy approach in combination with a confocal microscope, fast line scan imaging of fluorescent molecules allows precise extraction of diffusion coefficients ranging from below $0.1 \mu\text{m}^2/\text{s}$ up to hundreds of square micrometers per second ([Ries et al., 2009](#); [Hebert et al., 2005](#); [Figures 1B and S1](#); [STAR Methods](#)). Briefly, this approach yields the probability distribution function of an individual molecule occupying a given position in space and time (spatiotemporal image correlation spectroscopy [STICS] function); rapidly diffusing molecules can travel large distances in a short time, whereas bound or very slowly diffusing molecules persist at the same position for a long time. This method can capture combinations of different diffusion modes or of diffusion and binding, as illustrated schematically in [Figure 1C](#). We calibrated the method by using fluorescent compounds of known molecular weight, which yielded values in agreement with their theoretical diffusion coefficients in water ([Figure S1](#)).

To analyze cAMP dynamics in intact cells, we used this technology in HEK293 cells loaded with low concentrations ($<100 \text{ nM}$) of 8-FDA-cAMP ([Figure S2](#)). These experiments revealed that, at low cAMP levels, virtually all cAMP displays a pattern reflecting a bound (i.e., largely immobile) state of cAMP ([Figures 1D and S2D](#)). This can be appreciated qualitatively by the long-time tail of the STICS function ([Figures 1C, 1D, and S3](#)). This observation is striking because several studies have uniformly reported that cAMP diffuses very quickly in cells ([Table S1](#)). In stark contrast, our data suggest that, at basal concentrations, cAMP dynamics are severely constrained in cells.

Constrained cAMP diffusion in cells might be caused by cAMP binding to specific binding sites, resulting in “buffering.” To test whether such binding of 8-F-cAMP does indeed occur and would be overcome at higher cAMP concentrations by displacement from the binding sites, we stimulated HEK293 cells, after loading with 8-FDA-cAMP, with forskolin (fsk) ($10 \mu\text{M}$) and 3-isobutyl-1-methylxanthine (IBMX) ($100 \mu\text{M}$) to maximally elevate intracellular cAMP levels. Analysis of cAMP dynamics under these stimulated conditions reveals a strikingly different spatiotemporal pattern; the long-time tail of the STICS function was largely lost, whereas a broader opening at shorter times was observed ([Figures 1E, S2E, and S3](#)). This fast component can also be appreciated by looking at diffusion coefficients extracted from the rapid timescale of the mean square displacement (MSD) and also by looking at the average transit time of the molecules over a distance of $1 \mu\text{m}$ ([Figures 1F, S2E, and S2F](#)); this highlights

fast cAMP diffusion (tens up to hundreds of square micrometers per second) in fsk + IBMX-stimulated cells, similar to the diffusion speed of fluorescein. This is in stark contrast to cells under unstimulated conditions, where cAMP appears to be virtually immobile ([Figures 1D and 1F](#)).

An alternative possibility to explain restricted cAMP diffusion might be geometrical diffusion constraints in cells ([Richards et al., 2016](#)). To rule out a contribution of such constraints, we collected STICS functions for 8-F-cAMP dynamics in cytosolic preparations under basal conditions ([Figure 2A](#)) and after saturating binding sites with unlabeled cAMP ([Figure 2B](#)). A set of reference molecules was used, spanning a range of molecular weights of approximately three orders of magnitude: fluorescein alone ($\approx 0.3 \text{ kDa}$), EGFP ($\approx 25 \text{ kDa}$) ([Figure 2C](#)), and Epac1-camps-PDE4A1 ($\approx 120 \text{ kDa}$) ([Figure 2D](#)). The diffusion coefficients obtained are displayed in [Figure 2E](#) as a function of their molecular weights. Based on the diffusion coefficient of the heaviest molecule ($D = 27 \pm 2 \mu\text{m}^2/\text{s}$), we plotted the expected D values for the other molecules according to the Stokes-Einstein relationship, yielding the power law dependence $D = \text{molecular weight (MW)}^{-1/3}$ (dotted line). Interestingly, all molecules followed the expected free diffusion behavior, with the notable exception of 8-F-cAMP. Here the values are more than twice below the expected diffusion coefficient, indicating binding to heavier components of the cytosolic extracts, in the approximate average range of $10\text{--}50 \text{ kDa}$ (shaded area in [Figure 2E](#)). Strikingly, 8-F-cAMP recovered its free diffusion value upon addition of $100 \mu\text{M}$ unlabeled cAMP to block all presumed cAMP-binding sites in the cytosolic preparations ([Figures 2 and S3](#)).

Such immobilization of cAMP requires a high cAMP buffering capacity, and, in fact, for the main cAMP effector PKA, such sites have been reported to occur in cell lysates in the low micromolar range ([Walker-Gray et al., 2017](#)). To quantify all cAMP binding sites, we estimated the buffering capacity of cytosolic preparations of HEK293 cells by titrating the concentration of 8-F-cAMP and determining the bound versus free ratio with steady-state anisotropy measurements ([STAR Methods](#); [Figure S4](#)). Measurements done at two different dilutions of the cytosolic preparations gave a range of cytosolic cAMP binding sites of $6\text{--}15 \mu\text{M}$ which is, as expected, larger than reported for PKA alone ([Walker-Gray et al., 2017](#)). The buffering capacity of entire cells (including particulate fractions, such as membranes, that are removed during cytosol preparations) is likely to be higher ([Corbin et al., 1977](#)). In our model, we make a conservative assumption of $20 \mu\text{M}$ cAMP binding sites ([Methods S2](#)).

Together, these data indicate very significant binding of cAMP to intracellular binding sites. Under basal conditions and concentrations, cAMP is mostly bound, but when it is displaced, it diffuses quickly, compatible with diffusion rates observed in earlier studies.

PDEs Generate Nanometer-Sized cAMP Gradients in Intact Cells

We and others have shown that observed cAMP gradients in cells require effective diffusion of cAMP to be restricted by orders of magnitude compared with what has been measured so far ([Rich et al., 2000, 2001](#); [Feinstein et al., 2012](#); [Lohse et al.,](#)

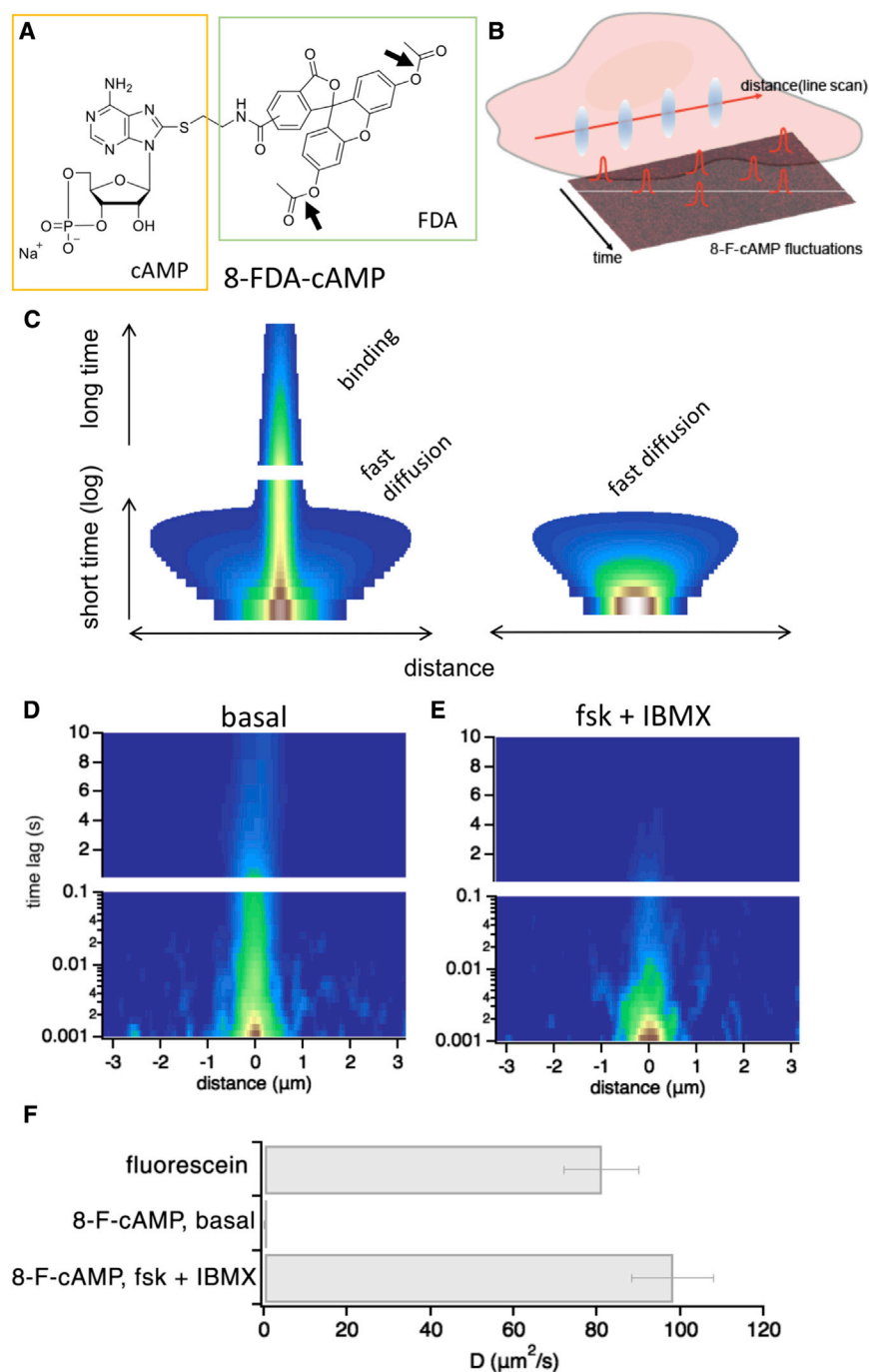


Figure 1. cAMP Dynamics Are Highly Restricted in Intact Cells

(A) Molecular structure of fluorogenic 8-FDA-cAMP. Arrows highlight sites where intracellular esterases cleave both ester bonds, resulting in the fluorescent molecule 8-F-cAMP.

(B) Line scan approach used in our experiments. The focused laser beam (blue ellipsoids) is scanned repeatedly along the cell cytosol, giving rise to a kymograph containing the 8-F-cAMP fluorescence fluctuations (STAR Methods).

(C) Two simulated STICS functions are illustrated schematically, referring to fast ($100 \mu\text{m}^2/\text{s}$) diffusion rates combined with binding (left) and fast diffusion rates alone (right). The x axis refers to the spatial and the y axis to the temporal dimension.

(D) Average STICS function (11 different cells, three independent experiments) measured in the cytoplasm of intact HEK293 cells loaded for 30 min with 100 nM 8-FDA-cAMP under basal conditions.

(E) Average STICS function (9 different cells, three independent experiments) measured in the cytoplasm of intact HEK293 cells loaded for 30 min with 100 nM 8-FDA-cAMP and stimulated for 5 min with fsk (10 μM)/IBMX (100 μM).

(F) Measured diffusion coefficient in HEK293 cells extracted from the slope of the MSD in the range of 0–0.5 ms for fluorescein, 8-F-cAMP (from D), and 8-F-cAMP stimulated with fsk + IBMX (from E). Error bars are standard deviations.

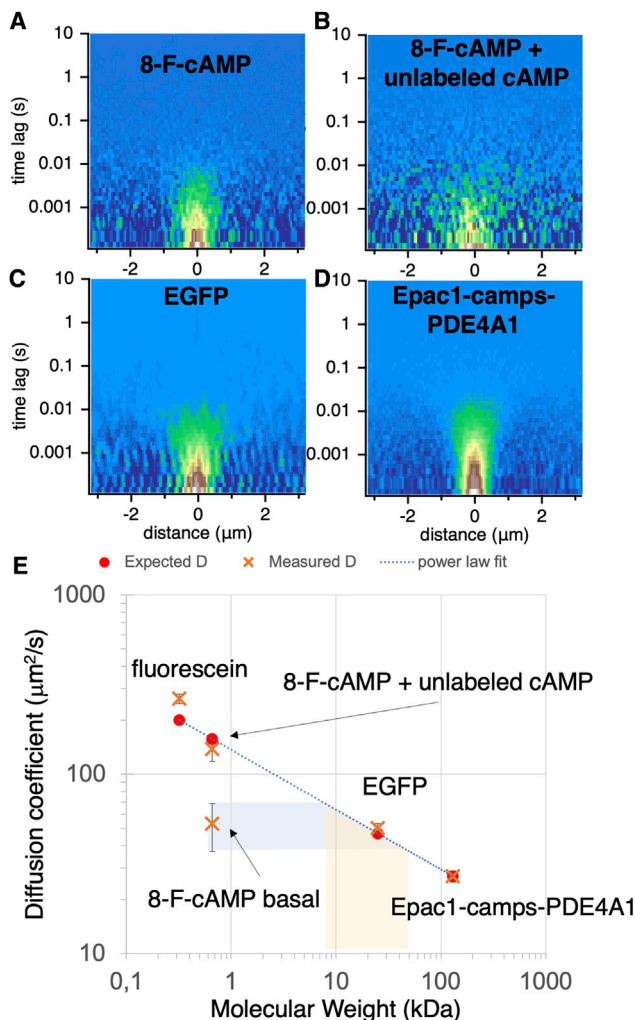


Figure 2. cAMP Dynamics Are Buffered via cAMP Binding Sites

(A) Average STICS function measured in a cytosol preparation of HEK293 cells loaded for 30 min with 100 nM 8-FDA-cAMP ($n = 8$).
(B) As in (A) after addition of unlabeled cAMP (100 μM) ($n = 6$).
(C and D) HEK293 cells expressing EGFP ($n = 6$) and (D) HEK293 cells expressing the fusion protein Epac1-camps-PDE4A1 ($n = 4$).
(E) Relationship between MW and diffusion coefficients. Orange crosses represent the diffusion coefficients extracted from the fit of the average STICS function (Equation 1; STAR Methods) derived from (A)–(D) and fluorescein alone. The diffusion coefficients are plotted against the MW of each compound. Red dots represent the theoretical diffusion coefficients based on the Stokes-Einstein relation $D = (KT/6\pi\eta R)$. The power law dependence on the MW (exponent = -0.3) is superimposed onto the data as a blue dotted line. Error bars are SEM.

2017; Xin et al., 2015). Our findings regarding cAMP dynamics (Figures 1 and 2) show that such restricted diffusion dynamics during the spatial spread of the cAMP signals does indeed exist because of cAMP buffering. We reasoned that the resulting reduction of free cAMP might resolve these discrepancies because they might facilitate the generation of local cAMP gradients by PDEs. This would provide the first direct experimental evidence of local cAMP gradient formation.

To visualize such gradients in intact cells and directly map their dimensions, we developed a set of genetically encoded fluorescence resonance energy transfer (FRET)-based cAMP nanorulers. Confocal images of all genetically encoded constructs in this study are compiled in Figure S5M. These sensors are composed of the FRET-based cAMP sensor Epac1-camps (Nikolaev et al., 2004) and a PDE, separated by single α -helical (SAH) domain linkers of defined nanometer length (Figures 3A and 3B). SAH domains are characterized by a modular sequence of ER/K amino acid repeats, resulting in a rod-like shape, which makes them ideally suited to spatially separate two protein moieties at a defined distance (Sivaramakrishnan and Spudis, 2011). Stimulation of endogenous β -adrenergic receptors (β -ARs) with isoproterenol in intact HEK293 cells led to an increase in cytosolic cAMP, as measured by Epac1-camps (Figure 3C). Tethering a PDE4A1 directly to Epac1-camps completely blunted the isoproterenol-induced FRET response (Figure 3E). This must be specifically due to the tethered PDE4A1 activity because, first, the specific PDE4 inhibitor roflumilast induced a large and robust FRET change in the Epac1-camps-PDE4A1 sensor (Figure 3E), and second, stoichiometric overexpression of PDE4A1 with Epac1-camps without tethering them together still gave a robust (albeit dampened) FRET signal (Figures 3D and 3G). These data indicate that tethered PDE4A1 effectively depletes cAMP from the region surrounding the Epac1-camps sensor.

Strikingly, upon spatial separation of Epac1-camps and PDE4A1 by 10 nm (Epac1-camps-SAH10-PDE4A1), isoproterenol stimulation induced a FRET response of almost the same amplitude as that seen with stoichiometric overexpression of both proteins individually (Figures 3F and 3G). As expected, inhibition of PDE4 activity in all constructs eliminated cAMP gradients (Figure 3H).

As controls for these experiments, we established that all constructs were expressed equally well, that the described effects were similar at all expression levels (Figure S5E), and that fusion of PDE4A1 or SAH10-PDE4A1 did not affect the affinity of Epac1-camps for cAMP (Figure S5A), nor did fusion of SAH10 to PDE4A1 reduce catalytic activity (Figure S5B–S5D). We also showed that the effect of tethered PDE4A1 was lost in a catalytically inactive mutant (Figures S5F and S5G). The highly significant differences between tethered and non-tethered or spacer-separated PDE4A1 (Figure 3G) strongly indicate that PDE4A1 creates a region of low cAMP concentration with a radius that is clearly smaller than 10 nm. We therefore define this as a low-cAMP nanodomain.

Low-cAMP Nanodomains Are PDE Subtype Specific

We reasoned that the size of such low-cAMP nanodomains might be determined by the type of PDE. Although the PDE4 family studied above comprises high-affinity (low-micromolar) but low-turnover (1–5 cAMP/s) enzymes, the PDE2 family represents the fastest enzymes with regard to cAMP degradation (Bender and Beavo, 2006). Therefore, we fused a truncated version of PDE2A3, PDE2cat, comprising only its catalytic domain (amino acids [aa] 578–941), to Epac1-camps, generating Epac1-camps-PDE2cat. In line with the findings obtained with PDE4, tethered PDE2cat activity blunted the cAMP-FRET response to isoproterenol in relation to Epac1-camps alone

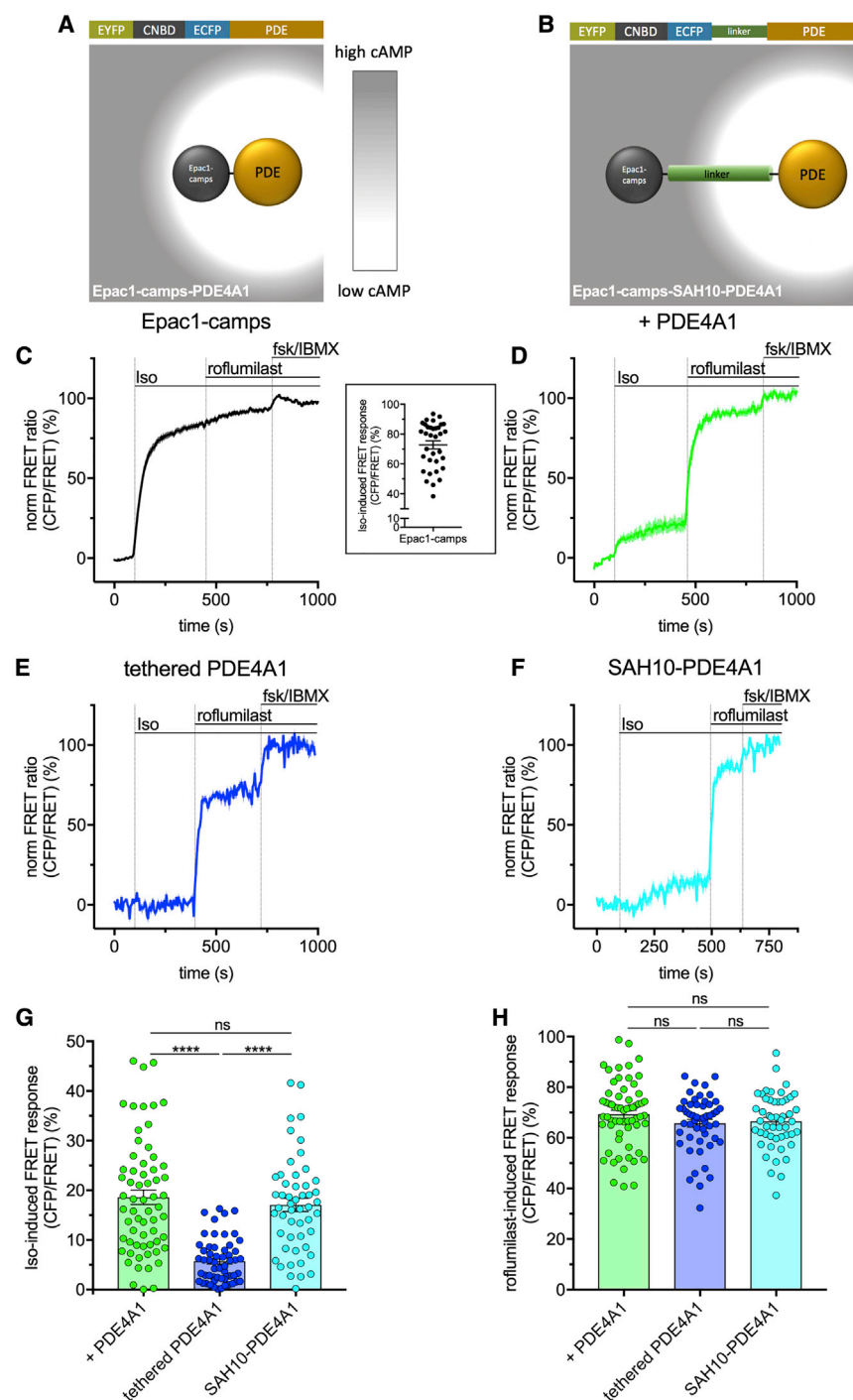


Figure 3. Genetically Encoded Nanorulers Map cAMP Gradients around Single PDE Molecules in Intact Cells

(A and B) Design of FRET-based nanorulers to identify low-cAMP nanodomains in intact cells. Tethering the FRET-based cAMP sensor Epac1-camps to a PDE allows measuring cAMP concentrations in the direct vicinity of a single PDE molecule (A). Incorporation of nanometer linkers based on SAH domains between Epac1-camps and a PDE allows measuring the cAMP gradient at defined distances away from the PDE (B). (C) Isoproterenol (Iso; 10 μ M) stimulation leads to an increase in cAMP levels that is detected by Epac1-camps (note upward-reflected trace).

(D) When Epac1-camps and PDE4A1 are expressed at equimolar levels but not tethered, a rise in cAMP levels is still detected upon Iso stimulation.

(E) However, when tethering PDE4A1 to Epac1-camps (which measures cAMP levels in the direct vicinity of PDE4A1), no rise in cAMP is detected upon Iso stimulation.

(F) Separating Epac1-camps and PDE4A1 with a 10-nm linker leads to a similar response as observed in the equimolar expression in (D).

(C–F) Average traces of corrected and normalized FRET ratios in HEK293 cells transfected with Epac1-camps (C), Epac1-camps-IRES2-PDE4A1 (i.e., individual but roughly equimolar expression of sensor and PDE) (D), Epac1-camps-PDE4A1 (tethered) (E), and Epac1-camps-SAH10nm-PDE4A1 (10-nm distance) (F), treated consecutively with Iso (10 μ M), the PDE4 inhibitor roflumilast (300 nM), and fsk (10 μ M)/IBMX (100 μ M). Traces are representative of 8, 13, 19, and 14 independent experiments, respectively. The solid lines indicate the mean and shaded areas the SEM. FRET traces are normalized to baseline (set to 0%) and maximal stimulation upon fsk + IBMX treatment (set to 100%). The inset in (C) shows the normalized, Iso-induced FRET ratios from all cells expressing Epac1-camps ($n = 34$).

(G and H) Normalized Iso-induced (G) or roflumilast-induced (H) FRET ratios pooled from all cells measured as in (D)–(F). $n = 63$ (Epac1-camps-IRES2-PDE4A1), 56 (Epac1-camps-PDE4A1), and 51 (Epac1-camps-SAH10nm-PDE4A1) cells. The columns represent means and the vertical bars SEM. **** $p < 0.0001$, one-way analysis of variance (ANOVA, Tukey's post-test); n.s., not significant.

(Figure 4A versus 4C). Only upon specific inhibition of PDE2 with BAY 60-7550 did Epac1-camps-PDE2cat detect an isoproterenol-mediated cAMP increase (Figure 4C). Stoichiometric expression of Epac1-camps and PDE2cat individually still led to a robust FRET signal upon isoproterenol stimulation (Figure 4B). These data confirm that the tethered PDE2 activity generates a low-cAMP nanodomain in its immediate vicinity (Figure 4E).

We then designed another cAMP nanoruler, Epac1-camps-SAH30-PDE2cat, which records cAMP levels at 30-nm distance to PDE2cat (Figure 4D). In contrast to the observations with Epac1-camps-SAH10-PDE4A1, we found a still significant effect on cAMP levels at 30-nm distance from PDE2cat (Epac1-camps-SAH30-PDE2cat) (Figures 4D and 4E). As expected, inhibition of PDE2 activity in all constructs eliminated cAMP gradients (Figure 4F). To account for the higher catalytic activity of PDE2cat than of PDE4A1, the PDE2cat experiments were performed at lower expression levels (Figure S5H). Again,

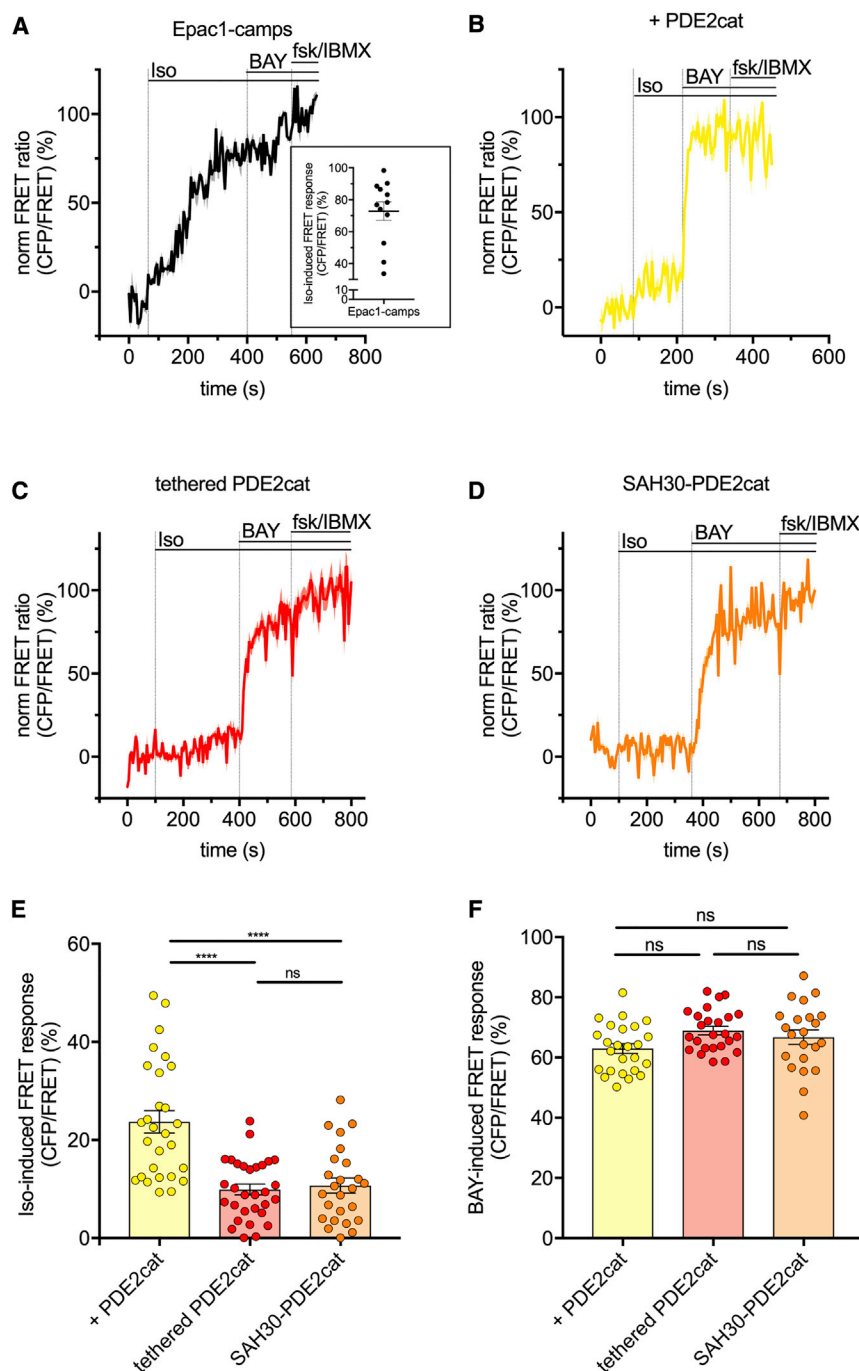


Figure 4. Low-cAMP Nanodomains Are PDE Subtype Specific

(A) Iso stimulation leads to an increase in cAMP levels that is detected by Epac1-camps (note the upward-reflected trace).

(B) When Epac1-camps and PDE2cat are expressed at equimolar levels but not tethered, a rise in cAMP levels is still detected upon Iso stimulation.

(C) However, when tethering PDE2cat to Epac1-camps, no rise in cAMP levels is detected upon Iso stimulation.

(D) Separating Epac1-camps and PDE with a 30-nm linker leads to almost no Iso-induced FRET response, similar to what is observed in (C).

(A–D) Average traces of corrected and normalized FRET ratios in HEK293 cells transfected with Epac1-camps (A), Epac1-camps-IRES2-PDE2cat (leading to individual but roughly equimolar expression of the two proteins) (B), Epac1-camps-PDE2cat (tethered) (C), and Epac1-camps-SAH30nm-PDE2cat (D), treated consecutively with Iso (10 μ M), the PDE2 inhibitor BAY 60-7550 (100 nM), and fsk (10 μ M)/IBMX (100 μ M). Traces are representative of 3, 10, 11, and 14 independent experiments, respectively. The inset in (A) shows the normalized Iso-induced FRET ratios from all cells expressing Epac1-camps ($n = 12$). The solid lines indicate the mean and shaded areas SEM. FRET traces are normalized to baseline (set to 0%) and maximal stimulation upon fsk + IBMX treatment (set to 100%).

(E and F) Normalized Iso-induced (E) and BAY 60-7550-induced (F) FRET ratios pooled from all cells measured as in (B)–(D). $n = 28$ (Epac1-camps-IRES2-PDE2cat), 30 (Epac1-camps-PDE2cat), and 25 (Epac1-camps-SAH30nm-PDE2cat) cells. The columns represent means and the vertical bars SEM. **** $p < 0.0001$, ANOVA, Tukey's post-test.

endogenous buffers and to progressively “flood” the small domains and, ultimately, entire cells.

We then aimed to assess whether such low-cAMP nanodomains might also be demonstrated in cytosolic preparations and to quantify the concentration threshold at which they might become flooded because PDEs are no longer able to establish significant cAMP gradients (Figure 5). Concentra-

tion-effect curves of cAMP-induced FRET changes of Epac1-camps are shown for the same conditions and constructs as used in cells for PDE4A1 (Figure 5A) and PDE2cat (Figure 5B), and the resultant shifts of the half maximal effective concentration (EC_{50}) values are given in Figure 5C. These data show, for Epac1-camps, an apparent cAMP affinity of 2.5 μ M, which is shifted to 10-fold higher concentrations by tethered PDE4A1, whereas individual stoichiometric expression of Epac1-camps and PDE4A1 only caused a 2-fold

we also showed that Epac1-camps-PDE2cat and Epac1-camps-SAH30-PDE2cat sensors were not compromised with regard to cAMP affinity (Figure S5I) or PDE catalytic activity (Figures S5J–S5L).

Combined, our data suggest that, under basal conditions, cells are able to buffer most of their cAMP. This, in turn, allows PDEs to generate low-cAMP nanodomains. Only upon stimulation of adenylyl cyclases (ACs) and inhibition of PDEs is the level of cAMP raised sufficiently to overcome the capacity of the

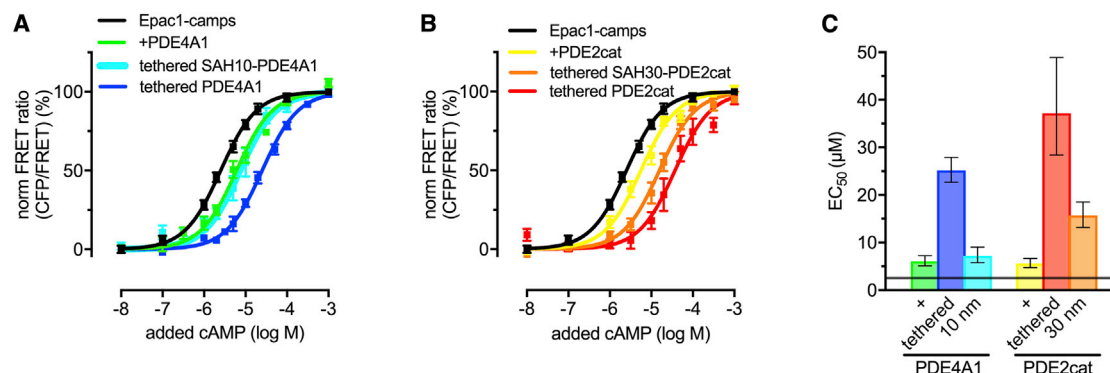


Figure 5. Low-cAMP Nanodomains Stay Intact in Cytosolic Cell Preparations and Become Flooded at Micromolar cAMP

(A and B) Shown are concentration-effect curves of cAMP-induced changes in FRET ratio normalized to buffer (set to 0%) and 1 mM cAMP (set to 100%). Data are means \pm SEM of at least three independent experiments.

(A) Tethering PDE4A1 (blue curve) to Epac1-camps (black curve) leads to a pronounced right-shift of the concentration-effect curve, much more than stoichiometric overexpression of Epac1-camps and PDE4A1 (+PDE4A1, green curve). The difference in the EC₅₀ values between the green (global PDE activity) and blue curves (local PDE activity) is a biochemical equivalent to the cAMP nanodomain. Separating Epac1-camps and PDE4A1 by 10 nm (Epac1-camps-SA10nm-PDE4A1) does not generate a low-cAMP nanodomain (turquoise curve). Note that the turquoise curve (cAMP at 10-nm distance from the PDE) and the green curve (global PDE activity) are superimposable.

(B) Tethering PDE2cat (red curve) to Epac1-camps (black curve) leads to a pronounced right-shift of the concentration-effect curve, significantly more than individual stoichiometric expression of Epac1-camps and PDE2cat (yellow curve). Separating Epac1-camps and PDE2cat by 30 nm (Epac1-camps-SA130nm-PDE2cat, orange curve) only partially restores the cAMP gradient. Note that the orange line (cAMP at 30-nm distance from the PDE) is between the yellow (global PDE activity) and red lines (local PDE activity).

(C) Apparent cAMP EC₅₀ values derived from the data in (A) and (B). The mean EC₅₀ of Epac1-camps is shown as a solid black line. Bars show the mean cAMP EC₅₀ values for stoichiometric expression of Epac1-camps plus PDE4A1/PDE2cat expressed separately (+), with tethered PDE4A1 or PDE2cat, respectively (tethered), and at a distance of 10 and 30 nm from the PDEs. Error bars show the 95% confidence intervals of the mean.

affinity shift (Figures 5A and 5C). In line with the results obtained in intact cells, separating PDE4A1 from Epac1-camps by 10 nm reduced the shift to almost the same level as stoichiometric expression, essentially abolishing the specific nanodomains (Figures 5A and 5C). Analogous experiments performed with PDE2cat revealed a somewhat larger (15-fold) shift for the directly tethered PDE, and here, as in cells, a 30-nm spacer only partially reduced the shift (Figures 5B and 5C). Inspection of the curves shows that the shifts also exist at higher cAMP concentrations, suggesting that the low-cAMP nanodomains become fully flooded only at high concentrations of cAMP.

Low-cAMP Nanodomains Control Local PKA Activity

To investigate directly whether cAMP nanodomains translate into similarly targeted PKA signaling, we designed analogous targeted PKA activity reporters. Fusing PDE4A1 to the PKA FRET sensor AKAR4 completely suppressed detection of PKA activity in response to stimulation of HEK293 cells with isoproterenol, whereas AKAR4 alone gave a robust signal (Figures 6A–6D). This indicates that the PDE “protects” PKA in its immediate vicinity from cAMP stimulation.

To demonstrate that PDEs shape local PKA gradients, we used full-length PDE2A3. The long N terminus of PDE2A3 should separate the catalytic center of the PDE from N-terminally fused sensors by several nanometers (Pandit et al., 2009). In fact, this construct allowed the respective sensors to again detect isoproterenol-stimulated cAMP levels (Figure 6E) or PKA activity (Figure 6F). Interestingly, the constructs

detected a comparable relative level of cAMP and of PKA activity (Figure 6G), strongly suggesting that the amount of cAMP at a given location in the cell dictates the degree of local PKA activity.

As controls for these experiments, we showed that only inhibitors of the relevant tethered PDE lead to phosphorylation of the tethered PKA substrate, whereas inhibitors of other PDEs have no effect (Figure S6). These data confirm the specificity of our results and illustrate that individual PDEs regulate cAMP signaling specifically in their immediate vicinity.

Model of cAMP Signaling at the Nanoscale

To describe our findings in quantitative terms, we use a biophysical model for formation of cAMP gradients by PDEs at the nanoscale (Methods S2). Based on our experimental observations (Figures 1, 2, 3, and S4), this model analyzes the effects of binding sites on free cAMP concentrations in cells and on the spatial profile of cAMP gradients generated by PDE-mediated degradation.

The model confirms that cAMP gradients around PDEs are of nanometer size (Figure 7B; Methods S2). Figure 7B illustrates the free cAMP concentration at a distance from PDE4A1 (in red) superimposed on the experimental free cAMP concentration ranges measured by using our FRET sensors at the PDE, 10 nm away, and in the bulk of the cytosol. The concentration gradient follows the equation $[cAMP] = [cAMP]_{bulk}(1 - R_0/r)$, where $[cAMP]$ denotes the concentration of free cAMP, $[cAMP]_{bulk}$ the concentration of free bulk cAMP far from the PDE, r the distance from the PDE catalytic site, and R_0 is a

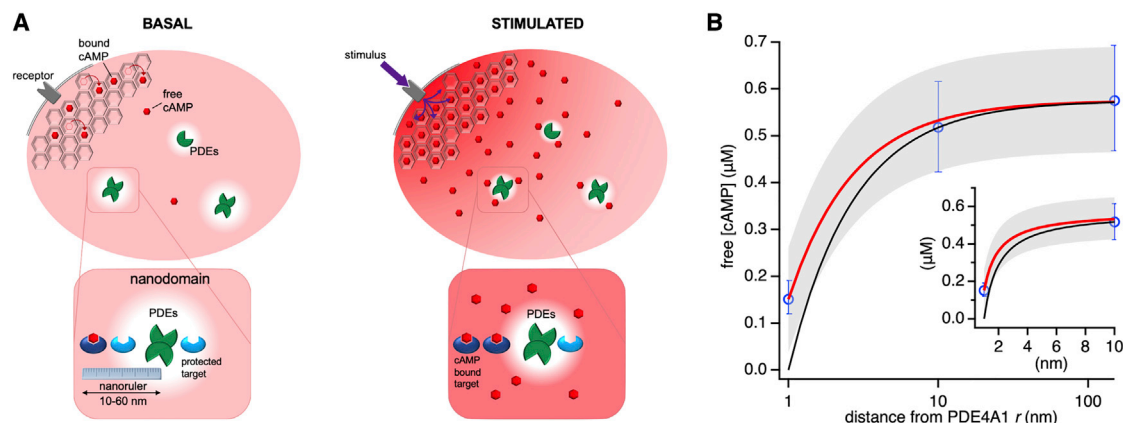


Figure 7. Model of cAMP Signaling at the Nanoscale

(A) Schematic illustration of buffered diffusion of cAMP and formation of low-cAMP nanodomains under basal (left) and stimulated conditions (right). The presence of a large concentration of cAMP binding sites (illustrated as honeycombs) (Figure S4) lowers the concentration of free cAMP (red dots). The low concentration of free cAMP enables PDEs to establish nanometer-size domains where the local cAMP concentration is decreased to a range below the activation threshold of local cAMP effectors (bottom). Upon stimulation (right), cAMP binding sites become progressively saturated, and, as a consequence, the width and depth of these nanodomains are decreased, eventually leading to flooding and activation of local cAMP effectors.

(B) The spatial cAMP concentration profile (red line) around a PDE4A1 molecule as inferred from experiments (Figure 3) and quantitative considerations (Methods S2). The red line shows the free cAMP concentration profile generated by a PDE4A1 dimer with a turnover rate of ~160 molecules per s by a single PDE4A1. The gray shaded area illustrates the range of possible profiles from experimental values (Methods S2). The open blue circles represent the measured mean values of free cAMP concentration at the PDE4A1 (data from Figure 3E), at 10-nm distance of the PDE (data from Figure 3F), and in bulk cytosol (data from Figure 3D). Error bars represent 95% confidence intervals. The black line indicates the cAMP concentration profile around a perfect absorber (Methods S2; Equation 3). The inset shows the same data with a linear x axis.

DISCUSSION

Despite a wealth of indirect evidence that cAMP compartments might exist in cells and should be under the control of PDEs, the molecular basis of how cAMP might be sequestered in cells has remained unknown for decades. Here we provide the molecular mechanisms of such cAMP compartmentation at the nanoscale.

Our data introduce the novel concept that cellular cAMP is governed by catch-and-release or buffered dynamics (Figure 7A). Under basal conditions, cAMP is mostly bound and effectively diffuses very slowly, if at all, and its free concentration is well below the levels of total cAMP; i.e., the levels measured by the usual biochemical assays. When cAMP molecules are released from the binding sites, they diffuse fast, compatible with diffusion rates observed previously, but are re-captured quickly by the next cAMP binding proteins (Figure 7A, left). This is entirely compatible with earlier experiments by us (e.g., Nikolaev et al., 2004) and others (Table S1), showing that rapid diffusion refers to the first time point where a stimulus can be noticed in different areas of a cell; however, the corresponding signals continue to increase for a long time thereafter, compatible with continued production of cAMP and its slow effective diffusion. The experimental approach we apply here has the advantage of using, for the first time, only trace amounts of fluorescent cAMP, not only allowing direct tracking of cAMP dynamics (as opposed to indirect tracking using FRET reporters) but also allowing measurements at or near basal cAMP levels, which permits us to clearly demonstrate buffered diffusion.

When cAMP levels are increased (for example, by receptor stimulation), the binding sites become progressively saturated, free cAMP increases, and diffusion occurs first from one binding

site to the next and, ultimately, when the binding sites become saturated, by free diffusion (Figure 7A, right panel). Buffering of the initial cAMP wave ensures that free cAMP levels are kept in a range that then permits individual PDEs to create and “defend” a nanometer-sized space around them with an even lower concentration of cAMP, allowing effectors such as PKA to be “protected” from external cAMP-mediated stimuli within these nanometer-size domains. Under these conditions, our data indicate that PDE catalytic rates are sufficient to metabolize the few free cAMP molecules that are present in these small volumes; when the ambient cAMP concentrations increase, the low cAMP domains become smaller. The downstream consequence of these nanometer-size regions of low cAMP is that PKA (and, presumably, other cAMP effectors) remain insensitive to cAMP signals until cAMP is increased to levels that are sufficient to progressively fill these regions (Figure 7A).

For our buffered diffusion model to hold, the requirement is that the buffering capacity of the cytoplasm is sufficient. In agreement with recent determinations (Walker-Gray et al., 2017), we directly determined the number of cytosolic cAMP binding sites to be in the range of 6–15 μM. It has been shown that ~30%–50% of the total cellular PKA is immobile and associated with the particulate fraction we remove during our cytosol preparations (Corbin et al., 1977). Therefore, the total amount of cAMP binding sites in cells is likely to be even higher than quantified here in cytosolic preparations. The discovery of the biomolecular condensates described in an accompanying paper strikingly illustrates additional “sponges” for cAMP (Zhang et al., 2020 [this issue of *Cell*]) that effectively increase the buffering capacity of the cell. Together, these sites are sufficient to very significantly buffer cellular cAMP levels, much like buffering of

intracellular calcium, where a large number of bindings sites reduce the free concentration and the effective diffusion rate of calcium ions (Wagner and Keizer, 1994).

Calculation of a concentration gradient around a single PDE4A1 based on the Smoluchowski model (Smoluchowski, 1916; Rice, 1985; Methods S2) shows that a nanometer-size region of significantly lowered cAMP does indeed occur (Figure 7B). Given the largely dimeric PDE4A1 structure, our data therefore indicate that the measured cAMP concentration values in the bulk and at the tethered FRET sensor are in agreement with an individual PDE4A1 turnover rate of about 160 molecules/s. Although this is higher than values reported for the purified enzyme (Bender and Beavo, 2006), these latter values might well be reduced because of damage during purification, whereas ours are some of the first data providing individual PDE4 turnover rates in intact cells and, therefore, do not conflict with previous literature values. In fact, in intact cells, very high PDE activity has already been reported (Nikolaev et al., 2005). The excellent agreement of the data of the cAMP measurements in intact cells and in cytosolic preparations (Methods S2) further supports this conclusion.

The agreement of the size of low-cAMP nanodomains with that of PKA activity measured with the AKAR4 sensor suggests that nanometer-size PDE domains indeed modulate downstream target activation and might represent functional modules of cAMP signaling. The demonstration of such functional cAMP and PKA nanodomains is further in line with recent observations by super-resolution microscopy of PKA signaling hotspots with a diameter of 100–200 nm (Mo et al., 2017). To constrain PKA activity to such small domains requires that its catalytic subunit is rapidly recaptured by regulatory subunits after activation (Mo et al., 2017; Walker-Gray et al., 2017) or that PKA can function as an intact holoenzyme (Smith et al., 2017).

Our data with PDE2 demonstrate that longer-range effects of PDEs could also be possible for cAMP and PKA signals. The mechanisms of these longer-range effects need to be explored further, but we would like to note the possibility of a larger effective radius (possibly because of the fact that, in these experiments, we used only isolated catalytic domains of PDE2 unlikely to remain immobile in intact cells because of lack of targeting domains) or of more complex arrangements. However, the excellent agreement of the data from intact cells and cytosolic preparations suggests that these observations are indeed a property of our PDE2 constructs.

Our demonstration of sharp concentration gradients along with direct translation into graded PKA activity explains how cAMP can act very locally and, thus, trigger responses spatially limited at the nanometer scale. The very small size of cAMP domains strongly suggests that compartmentalized cAMP signaling is controlled in a stochastic manner by individual molecules of cAMP. This spatially tight control provides the basis for the physiologically important specificity of cAMP signaling. Disruption of local cAMP signaling has been suggested to be associated with a variety of diseases (Gold et al., 2013), such as heart failure (Nikolaev et al., 2010) and cancer (Zhang et al., 2020). Elucidation of the molecular basis of cAMP compartmentation now permits us to link disruption of cAMP compartmentation

to disease and, thus, to explore novel therapeutic strategies that are based on a cell's ability to orchestrate cAMP signaling in nanometer-size domains.

STAR★METHODS

Detailed methods are provided in the online version of this paper and include the following:

- KEY RESOURCES TABLE
- RESOURCE AVAILABILITY
 - Lead Contact
 - Materials Availability
 - Data and Code Availability
- EXPERIMENTAL MODEL AND SUBJECT DETAILS
- METHOD DETAILS
 - Synthesis of 8-FDA-cAMP and characterization of 8-F-cAMP
 - cDNAs and biosensor construction
 - 8-FDA-cAMP cell penetration assays
 - Calibration compounds for diffusion measurements
 - Collecting line scans in a confocal microscope
 - Extracting molecular diffusion
 - Model fitting to STICS functions
 - Interpretation of MSD at multiple timescales
 - Single-cell FRET measurements
 - FRET measurements in cytosolic preparations
 - Quantification of cAMP binding sites
 - Molecular brightness
 - Confocal microscopy
 - Biophysical model of cAMP signaling at the nanoscale
- QUANTIFICATION AND STATISTICAL ANALYSIS

SUPPLEMENTAL INFORMATION

Supplemental Information can be found online at <https://doi.org/10.1016/j.cell.2020.07.035>.

ACKNOWLEDGMENTS

We thank Dr. Frank Schwede (Biolog GmbH, Germany) for discussions regarding the design of 8-FDA-cAMP and all members of the Lohse lab for critical discussions. We are grateful to Dr. Carmine Di Rienzo for discussions and constructive input regarding data analysis. This work was supported by the European Research Council grant TOPAS to M.J.L. and by NIH MIRA (R35-GM126940) to S.S. A.B., P.A., and M.J.L. acknowledge funding by the Deutsche Forschungsgemeinschaft (DFG) (German Research Foundation) through SFB1423, project number 421152132, subproject C03 (P.A. and M.J.L.) and subproject C05 (A.B.), and through SFB688, subproject B08 (M.J.L.).

AUTHOR CONTRIBUTIONS

A.B., P.A., and M.J.L. conceived the project and designed the methodology. A.B., P.A., C.K., A.H., and S.E.A. conducted investigations and formal analyses. U.Z. provided guidance for cloning strategies. I.M. contributed to the design of the methodology. S.S. provided guidance for preparation and use of SAH linkers. M.F. developed the biophysical model. A.B., P.A., and C.K. prepared data visualization. A.B., P.A., and M.J.L. wrote the manuscript with edits from C.K. and M.F. M.J.L. initiated the project. A.B., P.A., M.F., and M.J.L. supervised the research. A.B. and M.J.L. administered the project.

DECLARATION OF INTERESTS

The authors declare no competing interests.

Received: November 8, 2019

Revised: March 30, 2020

Accepted: July 23, 2020

Published: August 25, 2020

REFERENCES

- Agarwal, S.R., Clancy, C.E., and Harvey, R.D. (2016). Mechanisms Restricting Diffusion of Intracellular cAMP. *Sci. Rep.* **6**, 19577.
- Annibale, P., and Lohse, M.J. (2020). Spatial heterogeneity in molecular brightness. *Nat. Methods* **17**, 273–275.
- Arrio-Dupont, M., Cribier, S., Foucault, G., Devaux, P.F., and d'Albis, A. (1996). Diffusion of fluorescently labeled macromolecules in cultured muscle cells. *Biophys. J.* **70**, 2327–2332.
- Bacskaï, B.J., Hochner, B., Mahaut-Smith, M., Adams, S.R., Kaang, B.K., Kandel, E.R., and Tsien, R.Y. (1993). Spatially resolved dynamics of cAMP and protein kinase A subunits in *Aplysia* sensory neurons. *Science* **260**, 222–226.
- Bathe-Peters, M., Gmach, P., Annibale, P., and Lohse, M.J. (2020). Linescan microscopy data to extract diffusion coefficient of a fluorescent species using a commercial confocal microscope. *Data Brief* **29**, 105063.
- Bender, A.T., and Beavo, J.A. (2006). Cyclic nucleotide phosphodiesterases: molecular regulation to clinical use. *Pharmacol. Rev.* **58**, 488–520.
- Börner, S., Schwede, F., Schlipp, A., Berisha, F., Calebiro, D., Lohse, M.J., and Nikolaev, V.O. (2011). FRET measurements of intracellular cAMP concentrations and cAMP analog permeability in intact cells. *Nat. Protoc.* **6**, 427–438.
- Brunton, L.L., Hayes, J.S., and Mayer, S.E. (1979). Hormonally specific phosphorylation of cardiac troponin I and activation of glycogen phosphorylase. *Nature* **280**, 78–80.
- Buxton, I.L., and Brunton, L.L. (1983). Compartments of cyclic AMP and protein kinase in mammalian cardiomyocytes. *J. Biol. Chem.* **258**, 10233–10239.
- Chen, C., Nakamura, T., and Koutalos, Y. (1999). Cyclic AMP diffusion coefficient in frog olfactory cilia. *Biophys. J.* **76**, 2861–2867.
- Conti, M., and Beavo, J. (2007). Biochemistry and physiology of cyclic nucleotide phosphodiesterases: essential components in cyclic nucleotide signaling. *Annu. Rev. Biochem.* **76**, 481–511.
- Corbin, J.D., Sugden, P.H., Lincoln, T.M., and Keely, S.L. (1977). Compartmentalization of adenosine 3':5'-monophosphate and adenosine 3':5'-monophosphate-dependent protein kinase in heart tissue. *J. Biol. Chem.* **252**, 3854–3861.
- Depry, C., Allen, M.D., and Zhang, J. (2011). Visualization of PKA activity in plasma membrane microdomains. *Mol. Biosyst.* **7**, 52–58.
- Di Rienzo, C., and Annibale, P. (2016). Visualizing the molecular mode of motion from a correlative analysis of localization microscopy datasets. *Opt. Lett.* **41**, 4503–4506.
- Di Rienzo, C., Gratton, E., Beltram, F., and Cardarelli, F. (2013). Fast spatiotemporal correlation spectroscopy to determine protein lateral diffusion laws in live cell membranes. *Proc. Natl. Acad. Sci. USA* **110**, 12307–12312.
- Feinstein, W.P., Zhu, B., Leavesley, S.J., Sayner, S.L., and Rich, T.C. (2012). Assessment of cellular mechanisms contributing to cAMP compartmentalization in pulmonary microvascular endothelial cells. *Am. J. Physiol. Cell Physiol.* **302**, C839–C852.
- Gibson, D.G., Young, L., Chuang, R.Y., Venter, J.C., Hutchison, C.A., 3rd, and Smith, H.O. (2009). Enzymatic assembly of DNA molecules up to several hundred kilobases. *Nat. Methods* **6**, 343–345.
- Gold, M.G., Gonen, T., and Scott, J.D. (2013). Local cAMP signaling in disease at a glance. *J. Cell Sci.* **126**, 4537–4543.
- Hayes, J.S., Brunton, L.L., and Mayer, S.E. (1980). Selective activation of particulate cAMP-dependent protein kinase by isoproterenol and prostaglandin E1. *J. Biol. Chem.* **255**, 5113–5119.
- Hebert, B., Costantino, S., and Wiseman, P.W. (2005). Spatiotemporal image correlation spectroscopy (STICS) theory, verification, and application to protein velocity mapping in living CHO cells. *Biophys. J.* **88**, 3601–3614.
- Herget, S., Lohse, M.J., and Nikolaev, V.O. (2008). Real-time monitoring of phosphodiesterase inhibition in intact cells. *Cell. Signal.* **20**, 1423–1431.
- Houslay, M.D. (2010). Underpinning compartmentalised cAMP signalling through targeted cAMP breakdown. *Trends Biochem. Sci.* **35**, 91–100.
- Huang, R.C., and Gillette, R. (1993). Co-regulation of cAMP-activated Na⁺ current by Ca²⁺ in neurones of the mollusc *Pleurobranchaea*. *J. Physiol.* **462**, 307–320.
- Jameson, D.M., and Ross, J.A. (2010). Fluorescence polarization/anisotropy in diagnostics and imaging. *Chem. Rev.* **110**, 2685–2708.
- Lohse, C., Bock, A., Maiellaro, I., Hannawacker, A., Schad, L.R., Lohse, M.J., and Bauer, W.R. (2017). Experimental and mathematical analysis of cAMP nanodomains. *PLoS ONE* **12**, e0174856.
- Mika, D., Leroy, J., Vandecasteele, G., and Fischmeister, R. (2012). PDEs create local domains of cAMP signaling. *J. Mol. Cell. Cardiol.* **52**, 323–329.
- Mo, G.C., Ross, B., Hertel, F., Manna, P., Yang, X., Greenwald, E., Booth, C., Plummer, A.M., Tenner, B., Chen, Z., et al. (2017). Genetically encoded biosensors for visualizing live-cell biochemical activity at super-resolution. *Nat. Methods* **14**, 427–434.
- Nikolaev, V.O., Bünemann, M., Hein, L., Hannawacker, A., and Lohse, M.J. (2004). Novel single chain cAMP sensors for receptor-induced signal propagation. *J. Biol. Chem.* **279**, 37215–37218.
- Nikolaev, V.O., Gambaryan, S., Engelhardt, S., Walter, U., and Lohse, M.J. (2005). Real-time monitoring of the PDE2 activity of live cells: hormone-stimulated cAMP hydrolysis is faster than hormone-stimulated cAMP synthesis. *J. Biol. Chem.* **280**, 1716–1719.
- Nikolaev, V.O., Bünemann, M., Schmitteckert, E., Lohse, M.J., and Engelhardt, S. (2006). Cyclic AMP imaging in adult cardiac myocytes reveals far-reaching beta1-adrenergic but locally confined beta2-adrenergic receptor-mediated signaling. *Circ. Res.* **99**, 1084–1091.
- Nikolaev, V.O., Moshkov, A., Lyon, A.R., Miragoli, M., Novak, P., Paur, H., Lohse, M.J., Korchev, Y.E., Harding, S.E., and Gorelik, J. (2010). Beta2-adrenergic receptor redistribution in heart failure changes cAMP compartmentation. *Science* **327**, 1653–1657.
- Omori, K., and Kotera, J. (2007). Overview of PDEs and their regulation. *Circ. Res.* **100**, 309–327.
- Pandit, J., Forman, M.D., Fennell, K.F., Dillman, K.S., and Menniti, F.S. (2009). Mechanism for the allosteric regulation of phosphodiesterase 2A deduced from the X-ray structure of a near full-length construct. *Proc. Natl. Acad. Sci. USA* **106**, 18225–18230.
- Perera, R.K., and Nikolaev, V.O. (2013). Compartmentation of cAMP signalling in cardiomyocytes in health and disease. *Acta Physiol. (Oxf.)* **207**, 650–662.
- Rice, S.A. (1985). Diffusion-Limited Reactions. *Comprehensive Chemical Kinetics* (Elsevier).
- Rich, T.C., Fagan, K.A., Nakata, H., Schaack, J., Cooper, D.M., and Karpen, J.W. (2000). Cyclic nucleotide-gated channels colocalize with adenylyl cyclase in regions of restricted cAMP diffusion. *J. Gen. Physiol.* **116**, 147–161.
- Rich, T.C., Fagan, K.A., Tse, T.E., Schaack, J., Cooper, D.M., and Karpen, J.W. (2001). A uniform extracellular stimulus triggers distinct cAMP signals in different compartments of a simple cell. *Proc. Natl. Acad. Sci. USA* **98**, 13049–13054.
- Richards, M., Lomas, O., Jalink, K., Ford, K.L., Vaughan-Jones, R.D., Lefkimmiatis, K., and Swietach, P. (2016). Intracellular tortuosity underlies slow cAMP diffusion in adult ventricular myocytes. *Cardiovasc. Res.* **110**, 395–407.
- Ries, J., Chiantia, S., and Schwill, P. (2009). Accurate determination of membrane dynamics with line-scan FCS. *Biophys. J.* **96**, 1999–2008.
- Serfling, R., Seidel, L., Bock, A., Lohse, M.J., Annibale, P., and Coin, I. (2019). Quantitative Single-Residue Bioorthogonal Labeling of G Protein-Coupled Receptors in Live Cells. *ACS Chem. Biol.* **14**, 1141–1149.

- Sivaramakrishnan, S., and Spudich, J.A. (2011). Systematic control of protein interaction using a modular ER/K α -helix linker. *Proc. Natl. Acad. Sci. USA* **108**, 20467–20472.
- Smith, F.D., Esseltine, J.L., Nygren, P.J., Veasler, D., Byrne, D.P., Vonderach, M., Strashnov, I., Eysers, C.E., Eysers, P.A., Langeberg, L.K., and Scott, J.D. (2017). Local protein kinase A action proceeds through intact holoenzymes. *Science* **356**, 1288–1293.
- Smoluchowski, M.V. (1916). Drei Vorträge über Diffusion, Brownsche Bewegung und Koagulation von Kolloidteilchen. *Physik. Zeit.* **17**, 557–571, 585–599.
- Stangherlin, A., and Zaccolo, M. (2012). Phosphodiesterases and subcellular compartmentalized cAMP signaling in the cardiovascular system. *Am. J. Physiol. Heart Circ. Physiol.* **302**, H379–H390.
- Terrin, A., Di Benedetto, G., Pertegato, V., Cheung, Y.F., Baillie, G., Lynch, M.J., Elvassore, N., Prinz, A., Herberg, F.W., Houslay, M.D., and Zaccolo, M. (2006). PGE(1) stimulation of HEK293 cells generates multiple contiguous domains with different [cAMP]: role of compartmentalized phosphodiesterases. *J. Cell Biol.* **175**, 441–451.
- Wagner, J., and Keizer, J. (1994). Effects of rapid buffers on Ca^{2+} diffusion and Ca^{2+} oscillations. *Biophys. J.* **67**, 447–456.
- Walker-Gray, R., Stengel, F., and Gold, M.G. (2017). Mechanisms for restraining cAMP-dependent protein kinase revealed by subunit quantitation and cross-linking approaches. *Proc. Natl. Acad. Sci. USA* **114**, 10414–10419.
- Xin, W., Feinstein, W.P., Britain, A.L., Ochoa, C.D., Zhu, B., Richter, W., Leav- esley, S.J., and Rich, T.C. (2015). Estimating the magnitude of near-membrane PDE4 activity in living cells. *Am. J. Physiol. Cell Physiol.* **309**, C415–C424.
- Zaccolo, M. (2009). cAMP signal transduction in the heart: understanding spatial control for the development of novel therapeutic strategies. *Br. J. Phar- macol.* **158**, 50–60.
- Zaccolo, M. (2011). Spatial control of cAMP signalling in health and disease. *Curr. Opin. Pharmacol.* **11**, 649–655.
- Zhang, J.Z., Lu, T.W., Stolerman, L.M., Tenner, B., Yang, J.R., Zhang, J.F., Falcke, M., Rangamani, P., Taylor, S.S., Mehta, S., and Zhang, J. (2020). Phase Separation of a PKA Regulatory Subunit Controls cAMP Compartmentation and Oncogenic Signaling. *Cell* **182**, this issue, ■■■–■■■.

STAR★METHODS

KEY RESOURCES TABLE

REAGENT or RESOURCE	SOURCE	IDENTIFIER
Bacterial and Virus Strains		
NEB® 5-alpha Competent E.coli (High Efficiency)	New England Biolabs	Cat#C2987
XL1-Blue Competent Cells	Agilent	Cat#200249
Chemicals, Peptides, and Recombinant Proteins		
(-)-Isoproterenol hydrochloride	Sigma-Aldrich	Cat#I6504; CAS: 5984-95-2
3-isobutyl-1-methylxanthine (IBMX)	Sigma-Aldrich	Cat#I5879; CAS: 28822-58-4
8-FDA-cAMP	BIOLOG Life Science Institute	N/A
Adenosine 3',5'-cyclic monophosphate sodium salt monohydrate (cAMP)	Sigma-Aldrich	Cat#A6885; CAS: 37839-81-9
BAY 60-7550	Cayman Chemical	Cat#10011135; CAS: 439083-90-6
Benzamidine	Sigma-Aldrich	Cat#12072; CAS: 618-39-3
CHAPS	Avanti Polar Lipids	Cat#850500P; CAS: 75621-03-3
Effectene Transfection Reagent	QIAGEN	Cat#301427
Fluorescein	ThermoFisher Scientific	Cat#10700795; CAS: 2321-07-5
Fluorescein diacetate	Sigma-Aldrich	Cat#F7378 CAS: 596-09-8
Fluorescein isothiocyanate-dextran 20 kDa	Sigma-Aldrich	Cat#FD20; CAS: 60842-46-8
Fluorescein isothiocyanate-dextran 250 kDa	Sigma-Aldrich	Cat#FD250S; CAS: 60842-46-8
Fluorescein isothiocyanate-dextran 70 kDa	Sigma-Aldrich	Cat#90718; CAS: 60842-46-8
Forskolin	BioTrend	Cat#AOB6380-5; CAS: 66575-29-9
Gibson Assembly® Master Mix	New England Biolabs (Gibson et al., 2009)	Cat#E2611
Phenylmethanesulfonyl fluoride (PMSF)	Sigma-Aldrich	Cat#P7626; CAS: 329-98-6
Phosphodiesterase, 3',5'-cyclic-nucleotide-specific from bovine brain	Sigma-Aldrich	Cat#P9529; CAS: 9040-59-9
Purified PKA R1alpha, human	Biaffin GmbH&co KG	Cat#PK-PKA-R1A025
Roflumilast	Tocris Bioscience	Cat#6641; CAS: 162401-32-3
Trypsin inhibitor from soybean	Sigma-Aldrich	Cat#T9003; CAS: 9035-81-8
Critical Commercial Assays		
PDElight™ HTS cAMP Phosphodiesterase Assay Kit	Lonza	Cat#LT07-600
PKA (Protein Kinase A) Colorimetric Activity Kit	ThermoFisher Scientific	Cat#EIAPKA
Experimental Models: Cell Lines		
HEK-tsA201 cells	Sigma-Aldrich	ECACC Cat#96121229
Oligonucleotides		
Primers for Cloning, see Table S2	This paper	N/A
Recombinant DNA		
PDE2A (NM_002599) Human Untagged Clone	OriGene Technologies	Cat#SC110970
Epac1-camps	Nikolaev et al., 2004	N/A
Epac1-camps-PDE4A1	Herget et al., 2008	N/A
Epac1-camps-PDE4A1 D352A	Herget et al., 2008	N/A
Epac1-camps-SAH10-PDE4A1	This paper	N/A

(Continued on next page)

Continued

REAGENT or RESOURCE	SOURCE	IDENTIFIER
Epac1-camps-IRES2-PDE4A1	This paper	N/A
Epac1-camps-PDE2A3	This paper	N/A
Epac1-camps-PDE2cat	This paper	N/A
Epac1-camps-SAH30-PDE2cat	This paper	N/A
Epac1-camps-IRES2-PDE2cat	This paper	N/A
pcDNA3-AKAR4	Dr. Jin Zhang (UC San Diego, USA) (Depry et al., 2011)	Addgene Plasmid #61619
AKAR4-PDE4A1	This paper	N/A
AKAR4-PDE2A3	This paper	N/A
SPASM sensor with 10 nm ER/K α -helix	Sivaramakrishnan and Spudich, 2011	N/A
SPASM sensor with 30 nm ER/K α -helix	Sivaramakrishnan and Spudich, 2011	N/A
Software and Algorithms		
GraphPad Prism software 7.0	GraphPad Software Inc.	https://www.graphpad.com/scientific-software/prism/
IGOR Pro 7	WaveMetrics	https://www.wavemetrics.com/products/igorpro
Customs STICS code	Serfling et al., 2019; Bathe-Peters et al., 2020	available upon request to the authors
FluorEssence	Horiba	https://www.horiba.com/en_en/products/detail/action/show/Product/fluorescence-1378/
VisiView® 4.0 imaging software	Visitron Systems	https://www.visitron.de/products/visiviewr-software.html

RESOURCE AVAILABILITY

Lead Contact

Further information and requests for resources and reagents should be directed to and will be fulfilled by the lead contact, Martin J. Lohse (m.lohse@mdc-berlin.de).

Materials Availability

Plasmids generated in this study are available from the authors upon request.

Data and Code Availability

The published article includes all datasets generated or analyzed during this study. For some data analysis we used a custom code/algorithm implemented in IGOR Pro, as previously published (Di Rienzo and Annibale, 2016; Serfling et al., 2019; Bathe-Peters et al., 2020), which is available from the authors upon request.

EXPERIMENTAL MODEL AND SUBJECT DETAILS

HEK-tsA201 cells (ECACC 96121229 from Sigma-Aldrich Chemie GmbH), indicated as HEK293 throughout the manuscript, were cultured in Dulbecco's modified Eagle Medium (DMEM) with 4.5 g/L glucose (PAN biotech, Aidenbach, Germany), 10% fetal bovine serum (Biocrom GmbH, Berlin, Germany), 100 U/ml penicillin, 100 μ g/mL streptomycin (Pen/Strep, GIBCO Life technologies, Carlsbad, CA, USA) and 2 mM-glutamine (PAN biotech, Aidenbach, Germany) at 37°C and 5% CO₂. Cells were passaged in T75 flasks (SARSTEDT, Nümbrecht, Germany) every 2-4 days when reaching a confluency of 80%–90%. Cells were routinely tested for mycoplasma contamination using MycoAlert™ Mycoplasma Detection Kit from Lonza (Basel, Switzerland). Cell lines were not contaminated with mycoplasma.

For single-cell FRET measurements HEK293 cells were plated on 24 mm glass coverslips (Fisher Scientific GmbH, Waltham, MA, USA) in 6-well-dishes (SARSTEDT, Nümbrecht, Germany) at a density of approximately 2×10^5 cells/mL. Transfection of plasmids (600 ng for Epac1-camps-based constructs, 300 ng for AKAR4-based constructs) was carried out 6 h after seeding using the Effectene Transfection Reagent (QIAGEN GmbH, Venlo, Netherlands) according to the manufacturer's instructions. After 18-24 h, cells were used for imaging.

For FRET measurements in cytosolic preparations, HEK293 cells were plated on 100 mm dishes (SARSTEDT, Nümbrecht, Germany) to give a density of approximately 50%–60%. 8 h later cells were transfected with a total amount of 20 μ g cDNA (10 μ g cDNA encoding the gene of interest and 10 μ g pcDNA3) using calcium phosphate precipitation. 48 h after transfection, cells were used for experiments.

METHOD DETAILS

Synthesis of 8-FDA-cAMP and characterization of 8-F-cAMP

The designed fluorogenic cAMP analog 8-(2-(5(6)-carboxyfluoresceindiacetate)-aminoethylthio)adenosine-3',5'-cyclic monophosphate (abbreviation: 8-FDA-cAMP) was custom-synthesized by Biolog Life Science Institute, Bremen, Germany (details in [Methods S1](#)). The identity and purity of 8-FDA-cAMP were assessed with mass spectrometry and HPLC, respectively, by Biolog Life Science Institute, Bremen, Germany (details in [Methods S1](#)).

8-F-cAMP (the de-esterified fluorescent analog of the membrane-permeable prodrug 8-FDA-cAMP) was used for the photophysical and biochemical characterization. To provide the photophysical characteristics of 8-F-cAMP, we recorded the absorption, excitation, and emission spectra of 8-F-cAMP (details in [Methods S1](#)). To determine the binding affinity of 8-F-cAMP to its binding protein PKA regulatory subunit I alpha (PKA-R1 α), we performed steady-state anisotropy measurements (details in [Methods S1](#)). To show that 8-F-cAMP activates downstream signaling, we used the PKA Colorimetric Activity Kit (ThermoFisher Scientific, Waltham, MA, USA) which reports on the activation of endogenous PKA in HEK293 cell lysates (details in [Methods S1](#)). To determine the stability of 8-F-cAMP toward hydrolysis by PDEs, we conducted PDE activity assays using a purified PDE from bovine brain and a colorimetric PDE assay (PDELight™, Lonza) (details in [Methods S1](#)).

cDNAs and biosensor construction

The cDNA encoding PDE2A (NM_002599) was purchased from OriGene, Rockville, MD, USA. The AKAR4 plasmid ([Depry et al., 2011](#)) was a kind gift of Dr. Jin Zhang (UC San Diego, USA) and a plasmid encoding the IRES2 sequence was kindly provided by Dr. Gary Lewin (MDC Berlin, Germany).

To generate Epac1-camps-SAH10-PDE4A1 (and Epac1-camps-SAH30-PDE4A1) the SAH10 (and SAH30) linkers were PCR amplified from plasmids encoding *systematic protein affinity strength modulation* (SPASM) sensors published previously ([Sivaramakrishnan and Spudich, 2011](#)), and BamHI and Ascl restriction sites were introduced using the following set of primers (SAH10: #1: 5'-AAAAAGGATCCGGAGAAGAGGAAGAGAAA-3', #2: 5'-AAAAAAGGCGCGCCAGAGCCCTTCTTCTTGCCTTTTC-3', priming sequence underlined, restriction sites in italics; SAH30: #3: 5'-AAAAAAGGATCCGGAGAAGAGGAAGAGAAGAAG-3', #4: 5'-AAAAAGGCGCGCCAGAGCCTCTTTGTTTCTTTCTGC-3'). PCR fragments were cut with BamHI and Ascl and cloned in frame between Epac1-camps and PDE4A1 using a variant of Epac1-camps-PDE4A1 ([Herget et al., 2008](#)) as vector. To generate Epac1-camps-PDE2A3, Epac1-camps-PDE2cat (amino acids 578-941 from PDE2A3), and Epac1-camps-SAH30-PDE2cat, the coding sequences of PDE2A3 and PDE2cat were PCR amplified and Ascl and NotI restriction sites were inserted by using the following set of primers, respectively (PDE2A3: #5: 5'-AAAAAAGGCGCGCCGGGCGAGGCATGCGGCCAC-3', #6: 5'-AAAAAAGCGGCCGCTCACTCAGCATCAAGGCT-3'; and PDE2cat: #7: 5'-AAAAAAGGCGCGCCTCCGACGATGAGTATACCAAACCTT-3', #8: 5'-AAAAAAGGCGCGCCTCCGACGATGAGTATACCAAACCTT-3'). The respective PCR products were cut with Ascl and NotI and cloned in frame into Epac1-camps-PDE4A1 and Epac1-camps-SAH30-PDE4A1 where the PDE4A1 sequence was cut out with Ascl and NotI. All constructs derived by restriction enzyme cloning were transformed and amplified in XL1-Blue competent E.coli (Agilent Technologies, Waldbronn, Germany).

AKAR4-PDE4A1 and AKAR4-PDE2A3 were generated by Gibson assembly using Epac1-camps-PDE4A1 and Epac1-camps-PDE2A3, respectively, as templates ([Gibson et al., 2009](#)). To generate AKAR4-PDE4A1, AKAR4 was PCR amplified using a pair of primers (#8: 5'-CTCACTATAGGGAGACCCAAGCTTTAAGGATCCCATGGTGAGCAAGGG-3', #9: 5'-CACCAAGGGCATGGATCCTCGATGTTGTGGCGGATCTT-3') and inserted upstream of PDE4A1 in its vector which was linearized with the following primers (#10: 5'-AAGATCCGCCACAACATCGAGGGATCCATGCCCTTGGTG-3', #11: 5'-CCCTTGCTCACCATGGGATCCTTAAAGCTTGGGTCTCCCTATAGTGAG-3'). To generate AKAR4-PDE2A3, AKAR4 was PCR amplified using another pair of primers (#12: 5'-GGGAGACCCAAGCTTAAGGATCCCATGGTGAGCAAG-3', #13: 5'-GCCGCATGCCTGCCCGCGCGCCTCTCGATGTTGTGGCGGAT-3') and inserted upstream of PDE2A3 in its vector which was linearized with the following primers (#14: 5'-ATCCGCCACAAATCGAGAGGCGCGCCGGGCGAGGCATGCGGC-3', #15: 5'-CTTGCTCACCATGGGATCCTTAAGCTTGGGTCTCCCTAT-3').

To generate Epac1-camps-IRES2-PDE4A1, the IRES2 sequence was PCR amplified with the indicated primers (#16: 5'-GACGAGCTGTACAAGTGAGGATCCGCCCTCTCCCTCCCCCCCCCTA-3', #17: 5'-GCAGAAGAAATCCACCAAGGGCATTGTGGCCATATTATCATCGTGTTC-3') and inserted in frame in between Epac1-camps and PDE4A1 in the construct Epac1-camps-PDE4A1 which was linearized with the following primers (#18: 5'-AAACACGATGATAATATGGCCACAATGCCCTTGGTGATTTCTTCTGC-3', #19: 5'-TAGGGGGGGGGGAGGGAGAGGGGCGGATCCTCACTTGTACAGCTCGTC-3'). Epac1-camps-IRES2-PDE2cat was generated following exactly the same strategy using the following primers (IRES2:#20: 5'-GACGAGCTGTACAAGTGAGGATCCAGGCGCGCCGCCCTCTCCCTCCCCCCCCCTA-3', #21: 5'-AAGTTTGGTATACTCATCGTCGGACATTGTGGCCAATTATCATCGTGTTC-3'; and linearization of Epac1-camps-PDE2A3: #22: 5'-AAACACGATGATAATATGGCCACAATGTCCGACGATGAGTATACCAAACCTT-3', #23: 5'-TAGGGGGGGGGGAGGGAGAGGGGCGCGCGCCTGGATCCTCACTTGTACAGCTCGTC-3'). For assembly of the PCR products the Gibson Assembly® Master Mix (New England Biolabs GmbH, Frankfurt, Germany)

was used according to the manufacturer's instructions. All constructs derived by Gibson cloning were transformed and amplified in NEB® 5-alpha Competent E.coli (New England Biolabs GmbH, Frankfurt, Germany).

All sequences were validated by automated sequencing of each construct by Eurofins (Luxembourg, Luxembourg) or LGC (Teddington, UK). Confocal images of HEK293 cells expressing all FRET-based constructs are compiled in [Figure S5](#).

8-FDA-cAMP cell penetration assays

8-FDA-cAMP and FDA cell penetration assays were performed using a 96-well plate reader (Neo2, Biotek, Bad Friedrichshall, Germany), measuring whole fluorescence emission per well at 505 nm upon 488 nm excitation. 50,000 cells/well were seeded, and 24 wells were measured, in three replicates, for each experimental condition. Cells were kept in HBSS buffer, where spontaneous conversion of FDA and 8-FDA-cAMP to their fluorescent form is negligible. Confocal images of HEK293 cells loaded with either FDA or 8-FDA-cAMP are found in [Figures S2B and S2C](#).

Calibration compounds for diffusion measurements

Fluorescein-labeled compounds of different molecular weight (fluorescein isothiocyanate-dextran of 20, 70kDa, and 250 kDa) were dissolved in water, and the pH was set to pH = 9 by addition of NaOH. To pre-activate FDA into fluorescein, ester bonds in FDA were broken by incubation at 37°C for 30 minutes at pH 9. Concentrations were determined by absorbance spectroscopy in a Thermo-Fisher Evolution300 spectrophotometer. Measurements were performed at a final compound concentration of 100 nM. Approximately 40 µL of solution were inserted into an imaging chamber formed by a #1.5 coverslip immobilized onto a glass slide by melting two parallel stripes of Parafilm (Bemis Company, Neenah, USA).

Collecting line scans in a confocal microscope

Linescans were acquired in a Leica SP8 confocal microscope (Leica Microsystems, Wetzlar, Germany), with a resonant scan head allowing 12 kHz line rate. Excitation was achieved using a white light laser, at the wavelengths of 488 nm. Excitation power was set to 10% of the maximal laser output (0.3 mW at 488 nm), and $2 \cdot 10^6$ lines were collected within the sample, with a length of 256 pixels and a pixel size of 50 nm. A 40x 1.4 NA objective was used. Detection was performed in photon counting mode using Leica hybrid detectors. For 8-FDA-cAMP linescan experiments cells were plated on 25 mm (#1.5) coverslips and loaded for 30 minutes with 100 nM 8-FDA-cAMP at 37°C. Cells were then washed three times in Hank's Balanced Salt Solution (HBSS) (ThermoFisher) and imaged in HBSS.

Extracting molecular diffusion

Statistical analysis of the fluorescence fluctuations present in a sequence of images or a kymograph allows constructing a spatial-temporal correlation plot, containing the average single molecule transit times between any two arbitrary positions along the scan line ([Ries et al., 2009](#); [Hebert et al., 2005](#); [Di Rienzo et al., 2013](#); [Di Rienzo and Annibale, 2016](#)). Such two-dimensional plots, namely Spatial-Temporal Image Correlation Spectroscopy (STICS) functions have two axes: a space and a time axis. The overall shape of the STICS function for diffusion is that of a 'plume', broadening in space as a function of time ([Figures 1A and S1A–S1C](#)). This broadening reflects the process of diffusion: the probability of finding a Brownian particle which is found at $x = 0$ for time $t = 0$ is a normal distribution of increasing variance as time elapses. The more rapid the broadening of the plume ([Figures S1A–S1C](#)), the more rapid the molecular diffusion process. Horizontal sections of the plot provide Mean Squared Displacement (MSD) information (i.e., broadening as a function of time) ([Figure S1D](#)). Vertical cross sections, known as average Pair Correlation functions, reflect the distribution of molecular transit times across a defined distance d ([Figure S1G](#)). These reflect the probability of finding a molecule at a given distance from its original position at time 0, after a time lag t . The position of the peak, reflecting the broadening of the STICS function, shifts to longer times as the diffusion coefficient decreases.

The temporal resolution of the measurement is determined by how rapidly the subsequent acquisitions of the same area (or line) are performed. In our setup, taking advantage of resonant scanners operating at 12 kHz, we could reach a temporal resolution of about 80 µs.

Determining faster ($> 100 \mu\text{m}^2/\text{s}$) diffusion is at the limit of this method, but it was possible to observe a convergence to previously measured cAMP diffusion values, viz. $135 \pm 20 \mu\text{m}^2/\text{s}$, by fitting progressively shorter time-lags. Furthermore, the distribution of rapid arrival times ([Figure S2G](#)) in forskolin/IBMX-stimulated cells further confirms the presence of a fast-moving component upon displacement, in the form of a peak at about 5 ms travel time over one µm.

Model fitting to STICS functions

Briefly, the $256 \times 2 \cdot 10^6$ kymograph is corrected for drifts and slow fluctuations using a random number addition detrending, within a moving window of approximately $250 \cdot 10^3$ lines, which corresponds to about 20 s. The fast Fourier transform (FFT) and its complex conjugate were then calculated, and their product was inverse FFTed to yield the autocorrelation function of the kymograph, namely the STICS function. We used a custom algorithm written in IGOR Pro (WaveMetrics), as previously described ([Serfling et al., 2019](#); [Di Rienzo and Annibale, 2016](#)). For pure diffusion, the equation describing the STICS Function reads as follows ([Ries et al., 2009](#)):

$$G(x, t) = \frac{\gamma}{(N \cdot D \cdot t + \sigma_0^2)} e^{-\left(\frac{t^2 + (x-x_0)^2}{4 \cdot D \cdot t + \sigma_0^2}\right)} \quad (\text{Equation 1})$$

With x and t being space and time, respectively, and γ the so-called gamma factor of the Point Spread Function (PSF) of the microscope, normally 0.35. N is the number of fluorescent molecules in the PSF, D the diffusion coefficient of the species and σ_0 the waist of the PSF (of the order of 250–300 nm for the wavelength used). For each given t , Equation 1 can also be used for a line by line fit of the STICS function (as described in Figure S1D), yielding the MSDs reported in Figure S1E, as graphically highlighted in Figure S1F.

In the case of two species displaying distinct concentrations and diffusion rates, the equation becomes (with 1 and 2 referring to each of the two species, respectively):

$$G_2(x, t) = \frac{\gamma}{(N1 \cdot D1 \cdot t + \sigma_0^2)} e^{-\left(\frac{t^2 + (x-x_0)^2}{4 \cdot D1 \cdot t + \sigma_0^2}\right)} + \frac{\gamma}{(N2 \cdot D2 \cdot t + \sigma_0^2)} e^{-\left(\frac{t^2 + (x-x_0)^2}{4 \cdot D2 \cdot t + \sigma_0^2}\right)} \quad (\text{Equation 2})$$

Interpretation of MSD at multiple timescales

When two species with distinct diffusion coefficients combine, e.g., a fast diffusing and a slow diffusing component/bound component, a fast broadening STICS function and a slow one overlap. Figures S2H and S2I illustrate how this reflects in terms of the measured STICS function and recovered MSD, respectively: a first rapid increase of MSD is followed by a decrease and again an increase, although at a slow pace. This should be interpreted in the following way: when the temporal resolution of the sampling is high enough, e.g., less than 10 ms as in Figure S2I, then rapid ‘jumps’ of the molecules can be appreciated. However, once the temporal resolution is lower, e.g., above 100 ms, then the fast jumps cannot be captured anymore, and we are in the domain where the slower diffusing species dominates the MSD. This simulated plot represents the scenario observed in Figure 1 for the fsk/IBMX stimulated cells, where a fraction of the 8-F-cAMP diffuses very rapidly, on the background of a major fraction that still moves very slowly.

Single-cell FRET measurements

Transfected HEK293 cells were transferred to imaging chambers (Attofluor™, ThermoFisher Scientifics), washed twice with FRET imaging buffer (144 mM NaCl, 5.4 mM KCl, 2 mM CaCl₂ (Carl Roth GmbH & Co. KG, Karlsruhe, Germany), 1 mM MgCl₂ (AppliChem, Darmstadt, Germany), 10 mM HEPES (Sigma-Aldrich Chemie GmbH); pH = 7.3). FRET measurements were carried out at room temperature using an epifluorescence microscope (Leica DMI8 inverted microscope, Leica Microsystems, Wetzlar, Germany) equipped with an oil immersion objective (HC PL APO 40x/1.30, Leica Microsystems, Wetzlar, Germany), a dichroic beam splitter (T505lpxr, Visitron Systems, Puchheim, Germany), a high-speed polychromator (VisiChrome, Visitron Systems), a Xe-Lamp (75W, 5.7 A, Hamamatsu Photonics, Hamamatsu City, Japan), a camera system (Photometrics Prime 95B CMOS camera, Visitron systems) with an Optosplit II dual emission image splitter (Cairn, Edinburgh, Scotland, UK) with CFP 470/24 and YFP 535/30 emission filters (Chroma Technology, Bellows Falls, VT, USA). Cells were brought into focus and regions of interest were drawn around single cells using the VisiView® 4.0 imaging software (Visitron Systems). Spatial homogeneity of the expression of the constructs was taken into account by ROI selection. In general, large ROIs containing most of the cell allow for averaging out any residual spatial heterogeneity within the cytosol. A time series of images was recorded every 5 s upon 100 ms exposure to 436 nm light. After reaching a stable baseline, cells were stimulated with the β -adrenergic agonist isoproterenol (Iso, 10 μ M), followed by specific PDE inhibition (300 nM roflumilast for PDE4A1 constructs, and 100 nM BAY 60-7550 for PDE2cat and PDE2A3 constructs). To reach maximal cAMP levels, a combination of fsk (10 μ M) and IBMX (100 μ M) were applied at the end of every experiment. Data from individual channels (CFP and YFP) were exported and corrected offline for background and bleedthrough (Börner et al., 2011). Inverted FRET ratios (CFP/FRET) were calculated and normalized to baseline (average of 10 data points before compound addition, set to 0% and fsk/IBMX (max cAMP response, set to 100%). After every experiment, direct YFP excitation at 505 nm (emission: 560 nm) was recorded to evaluate expression levels of the sensors.

FRET measurements in cytosolic preparations

Transfected HEK293 cells on a 10 cm plate (corresponding to approximately 1–1.5x10⁷ cells) were washed twice with ice-cold Dulbecco's Phosphate Buffered Saline (Sigma-Aldrich) and harvested in 300 μ L lysis buffer (10 mM Tris-HCl, 10 mM MgCl₂, pH 7.4) containing 1 mM PMSF and protease inhibitors (20 μ g/mL trypsin inhibitor from soybean and 60 μ g/mL benzamide). Cells were lysed by homogenization (two rounds of 10 s each using a T8 Ultra-Turrax® homogenizer (IKA, Staufen, Germany)). Nuclei and cell debris were spun down by centrifugation (1000xg, 5 min, 4°C). To obtain the cytosolic fraction, the supernatant was centrifuged again (100.000xg, 30 min, 4°C). The resultant supernatants were transferred to a quartz cuvette and adjusted with 10 mM Tris-HCl, 10 mM MgCl₂ (pH 7.4) to comparable sensor densities (assessed by direct YFP excitation). Fluorescence emission spectra were recorded with a LS50B spectrometer (PerkinElmer Life Sciences, Waltham, MA, USA) at 436 nm excitation, and emission was measured between 460 and 550 nm after adding increasing concentrations of cAMP. 480/525 nm FRET emission ratios were

calculated at different cAMP concentrations and fitted with a three-parameter logistic function and normalized to the lower (absence of cAMP; set 0%) and upper plateau (saturating concentrations of cAMP, set 100%) of the concentration-effect curves.

Quantification of cAMP binding sites

Cytosolic HEK293 cell preparations for the quantification of buffering capacities (Figure S4) were prepared as follows: HEK293 cells grown on a 10 cm dish, containing approximately 1×10^7 cells, were harvested in 300 μ L binding buffer (20 mM MOPS, 150 mM NaCl, 0.005% CHAPS, pH7) containing 1mM PMSF and protease inhibitors (20 μ g/mL trypsin inhibitor from soybean and 60 μ g/mL benzamide) and cytosolic extracts were prepared according to the protocol described above (FRET measurements in cytosolic preparations). Estimating an average cell volume of 1 pL per cell, the total cell volume of harvested cells (10 μ L) is diluted 30 times (30x) by addition of 300 μ L binding buffer for harvesting. For anisotropy measurements, 0.5 mM IBMX were added and the cytosolic preparation was further diluted twice or 50 times with binding buffer, resulting in a 60x or 1500x dilution, respectively. Steady state anisotropy (from here on only referred to as 'anisotropy') as well as fluorescence excitation and emission spectra were measured on a Horiba Yobin-Yvon Fluoromax Plus spectrophotometer using the appropriate routine of the FluorEssence software. 8-F-cAMP and fluorescein were both excited at 485 nm and fluorescence was measured at 535 nm. Slit width was 5 nm for both excitation and emission. 600 μ L of solution were pipetted in a quartz cuvette (Thorlabs). Integration time was set to between 1-10 s. Fluorescence intensity I was measured along all polarizations (I_{hh} , I_{hv} , I_{vh} , I_{vv}) and anisotropy r was calculated according to the standard equation (Jameson and Ross, 2010):

$$r = \frac{\frac{I_{vv}I_{hh}}{I_{hv}I_{vh}} - 1}{\frac{I_{vv}I_{hh}}{I_{hv}I_{vh}} + 2} \quad (\text{Equation 3})$$

When imaging scattering solutions (such as cytosolic cell extracts) anisotropy values were corrected to those of the pure solution - without any fluorescent dye added - by subtracting each of the corresponding fluorescence intensity values at each polarization.

Molecular brightness

Molecular brightness experiments were performed as previously reported (Annibale and Lohse, 2020). Briefly, movies of 100 frames of individual cells were acquired using a Laser Scanning Confocal Microscope SP8 (Leica), at a speed of 400 Hz, with an excitation power of 3% at 514 nm, corresponding to a few μ W in the sample plane. Detection was performed using photon counting detectors (Leica HyD), in the spectral range 520-600 nm. Molecular brightness values per pixel dwell time were calculated for each pixel, and the average cytosolic value from each individual cell is reported, after converting to photon counts/s. Briefly, molecular brightness is calculated by measuring the variance σ of the photon counts over time for each pixel by the average intensity value k , according to the formula: σ^2/k . The values of all the pixel within a homogeneous area of the cytosol are then averaged together.

Confocal microscopy

Fluorescence microscopy experiments were performed either on a Leica SP8 Confocal Microscopes, using HyD photon counting detectors and a White Laser light source to achieve excitation at the desired wavelengths (488 nm, and 514 nm). Emission was collected in the 500-600 nm and 520-600 nm range respectively. A 40x 1.3 NA objective was used, and the electronic zoom was set to achieve a pixel size of 50 nm.

Biophysical model of cAMP signaling at the nanoscale

We have modeled cAMP reaction/diffusion behavior in the cell, in particular in the vicinity of a PDE, according to the classical treatment original provided by Smoluchowski (1916); details in Methods S2. Here, the catalytic site of the PDE is seen as a sphere of radius R and cAMP as a species diffusing (with a diffusion coefficient D) in its vicinity, assuming that no cAMP sources are close by. The notion that the diffusion is buffered affects the free cAMP concentration $[cAMP]$, and in all our calculations the diffusion coefficient D refers to the free cAMP diffusion rate. This assumption is justified as we are interested in length scales of the order 30 nm, which is well below the average distance between two PDEs at physiological concentrations. Once the cAMP reaches the surfaces of the sphere, a degradation reaction takes place, making the PDE effectively a spherical sink characterized by a flux I of molecules degraded per unit time, in units of mol/s (or nmol/s or μ mol/s). The requirement that the total flux of free cAMP toward the PDE at the radius R equals the turnover I (Rice, 1985), leads to the relation

$$4\pi R^2 D \left. \frac{\partial [cAMP]}{\partial r} \right|_{r=R} = I. \quad (\text{Equation 4})$$

Which allows to solve the appropriate reaction-diffusion equation in spherical coordinates, leading to the following relation for $[cAMP]$ as a function of the distance r from the PDE

$$[cAMP](r) = [cAMP]_{bulk} - \frac{I}{4\pi D r}. \quad (\text{Equation 5})$$

The equation can also be written in terms of the radius R_0 where the concentration would be 0, i.e., the radius of a perfect absorber.

$$[cAMP](r) = [cAMP]_{bulk} \left(1 - \frac{R_0}{r} \right). \quad (\text{Equation 6})$$

QUANTIFICATION AND STATISTICAL ANALYSIS

Data analysis was performed using GraphPad Prism software 7.0 (GraphPad Software, San Diego, USA) and IGOR Pro 7 (Wavemetrics, Lake Oswego, USA). Normal distribution of data points was tested in every dataset using D'Agostino-Pearson omnibus normality test before evaluating significance. When comparing two populations, a Student's t test was used. When comparing three or more populations, a parametric one-way ANOVA with Tukey's multiple comparison test was used. The confidence interval was set to 95% (p value = 0.05). Significance was assessed as followed: ns (not significant) * $p \leq 0.05$; ** $p \leq 0.01$; *** $p \leq 0.001$, **** $p \leq 0.0001$. Data are represented throughout as mean \pm error (s.e.m., SD, or 95% confidence intervals), plus – where appropriate – as scatterplots of individual results. More details about statistics, e.g., repetition of experiments and cell numbers, are indicated in the respective figure legends.

Supplemental Figures

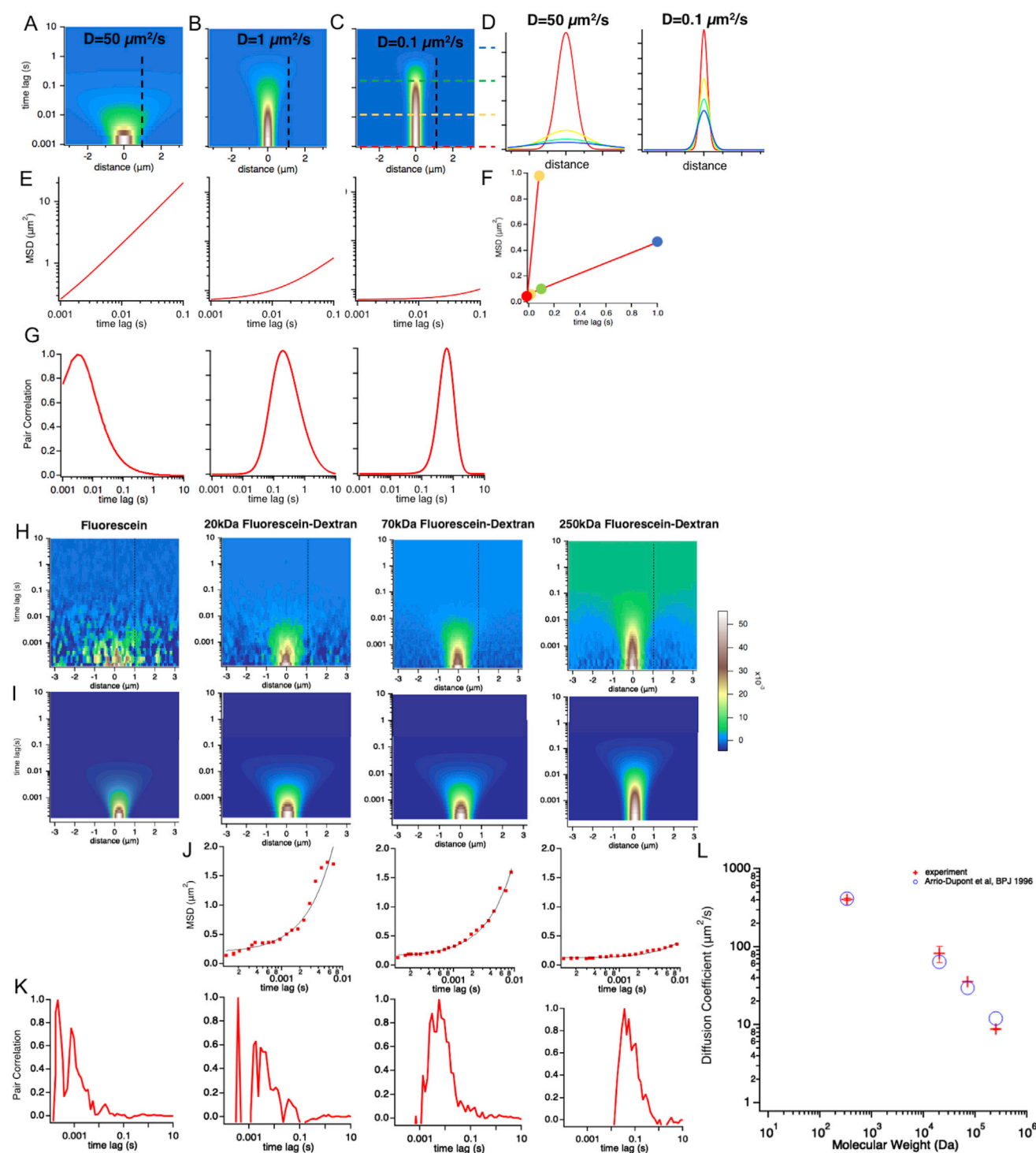


Figure S1. Concept of Measuring the Diffusion Coefficient of a Fluorescent Species Based on Sequential Rapid Line Scans and STICS Measurement of Diffusion of a Set of Reference Molecules of Known MW in Water: Experiments and Theory, Related to Figures 1 and 2
(A–C) Simulated STICS function derived for a species undergoing free diffusion in 3D at a rate of (A) $50 \mu\text{m}^2/\text{s}$, (B) $1 \mu\text{m}^2/\text{s}$, and (C) $0.1 \mu\text{m}^2/\text{s}$.

(legend continued on next page)

-
- (D) Measured (Gaussian) profiles of the STICS functions in (A) and (C) at four different times highlighted by the dashed lines, namely 1 ms (red), 10 ms (yellow), 100 ms (green) and 1 s (blue).
- (E) From the broadening of the Gaussians measured at increasing time lags, it is possible to reconstruct a MSD ([Equation 1](#)).
- (F) This approach is graphically summarized using a color code referring to the curves in (D).
- (G) Vertical cross sections of the STICS functions in (A), illustrating the shift to the right of the distribution of arrival times as the diffusion coefficient is reduced from $50 \mu\text{m}^2/\text{s}$ to $0.1 \mu\text{m}^2/\text{s}$.
- (H) Average STICS functions (3 independent experiments) of 100 nM fluorescein, 100 nM 20kDa fluorescein-dextran, 100 nM 70kDa fluorescein-dextran and of 100 nM 250kDa fluorescein-dextran measured in water. The pH was set to pH = 9 using NaOH and the measurements performed at room temperature ($T = 25^\circ\text{C}$).
- (I) Least-squares one-diffusion component fit ([Equation 1](#)) of the STICS functions displayed in (H).
- (J) Mean squared displacement (MSD) from the STICS functions in (H) (with exception of fluorescein, which is too fast for this line by line fitting and [Equation 1](#) was used).
- (K) Distribution of arrival times over a distance of $1 \mu\text{m}$ for FDA, 20 kDa, 70 kDa, 250 kDa fluorescein-dextran molecules respectively.
- (L) Red crosses display diffusion coefficients extracted from the data displayed in (H) as a function of the molecular weight. Blue circles represent the predicted diffusion coefficients for these molecules as derived from the literature ([Arrio-Dupont et al., 1996](#)).

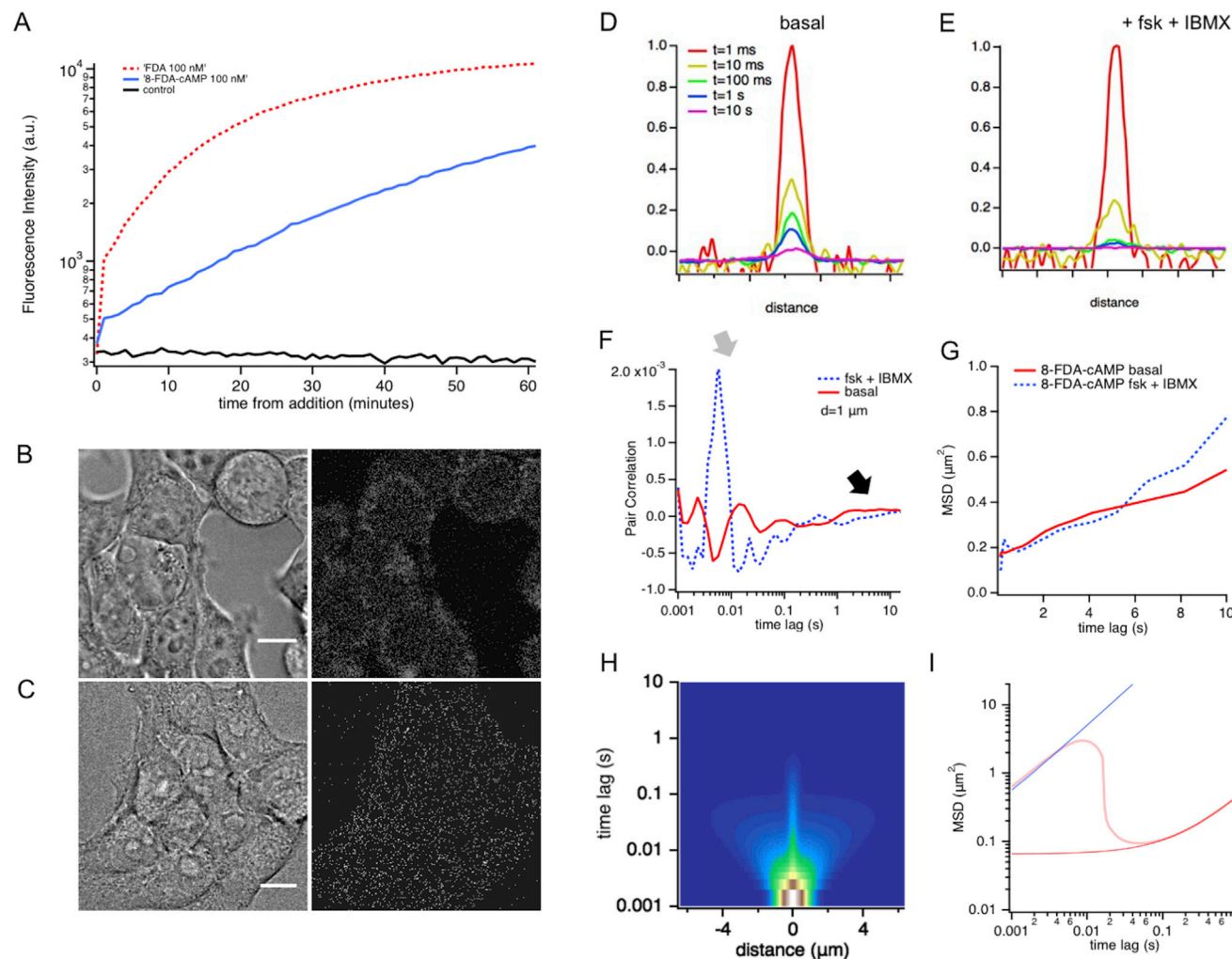


Figure S2. Cellular Uptake Kinetics and Distribution of FDA and 8-FDA-cAMP and Multi-scale cAMP Dynamics in Intact Cells, Related to Figure 1

(A) Fluorescence intensity time course recorded in a Neo2 plate reader (see STAR Methods) from a population of HEK293 cells incubated with 100 nM FDA (red), 100 nM 8-FDA-cAMP (blue), or HBSS (black), respectively.

(B and C) Confocal and corresponding DIC images of HEK293 cells loaded with 100 nM of 8-FDA-cAMP (B) or 100 nM FDA (C) after 30 min of incubation and washout in HBSS. Scale bars are 10 μm .

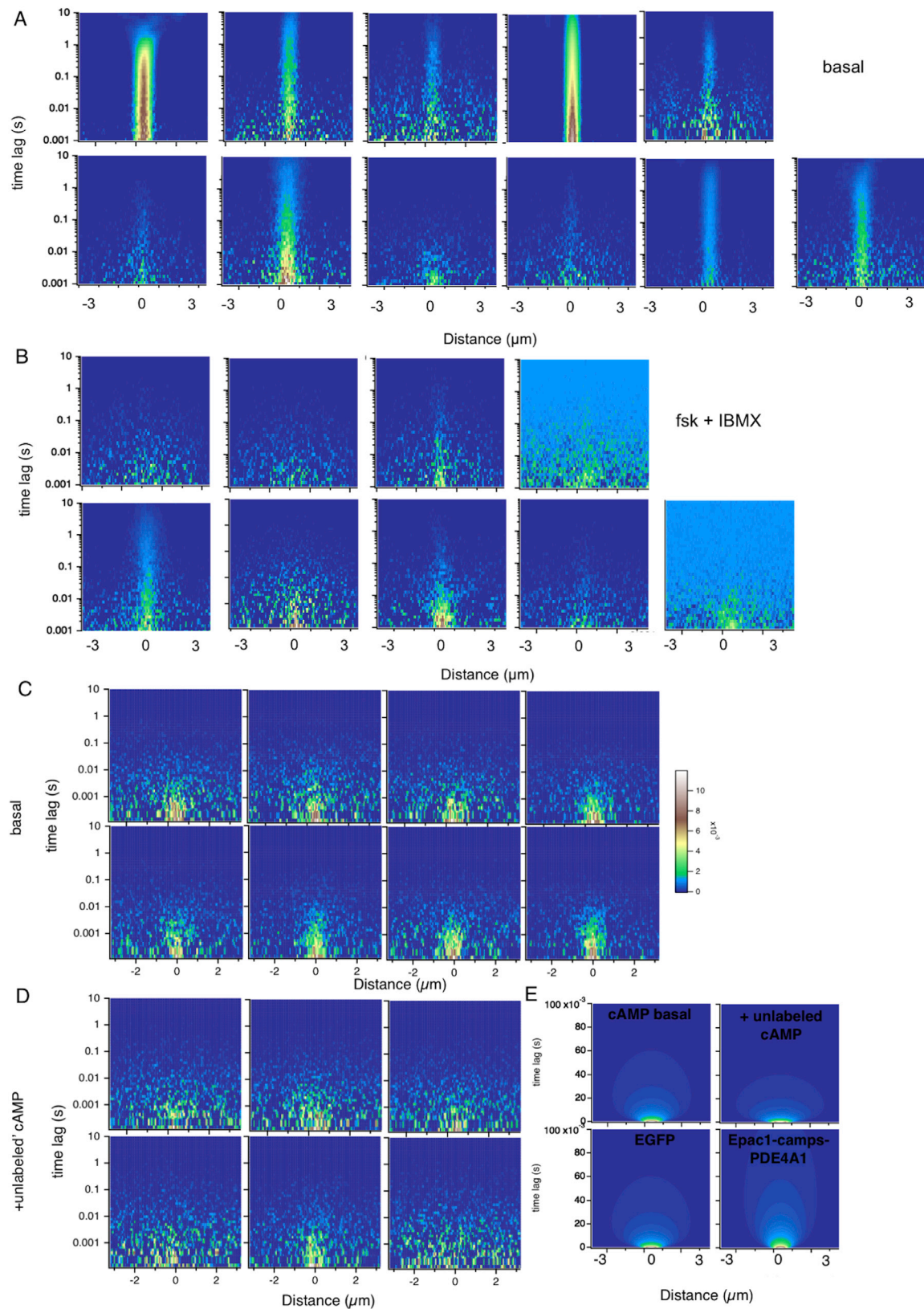
(D) The broadening of the STICS function in Figure 1D (basal) as a function of time is recorded by displaying its horizontal cross sections at selected time points, as indicated by the color scale.

(E) Same as in (D), for the STICS functions in Figure 1E (stimulated, i.e., fsk (10 μM)/IBMX (100 μM)).

(F) Distribution of average molecular arrival times extracted from the vertical profiles of Figures 1D and 1E at a distance of 1 μm .

(G) MSD for the basal and fsk/IBMX stimulated case for the 0–2 ms range.

(H) Simulated STICS function for the combined diffusion of (H) a fast (150 $\mu\text{m}^2/\text{s}$) and a slow (0.1 $\mu\text{m}^2/\text{s}$) component and (I) resulting MSD with linear fits to the two components: fast (blue), slow (red).



(legend on next page)

Figure S3. STICS Functions of 8-FDA-cAMP in Intact HEK293 Cells and Cytosolic Preparations, Related to Figures 1 and 2

(A) Shown are nine representative STICS functions for 8-F-cAMP dynamics in HEK293 cells under basal conditions.

(B) Shown are nine representative STICS functions for 8-F-cAMP dynamics in HEK293 cells after 5 min stimulation with fsk (10 μ M)/IBMX (100 μ M).

(C and D) Representative STICS functions for (C) 8-F-cAMP dynamics in HEK293 cell cytosolic preparations in basal conditions and (D) after addition of 100 μ M unlabeled cAMP.

(E) 2D least-squares fit to the STICS functions reported in Figures 2A–2D using Equation 1. The temporal axes of fits are reported in linear scale, to facilitate comparison.

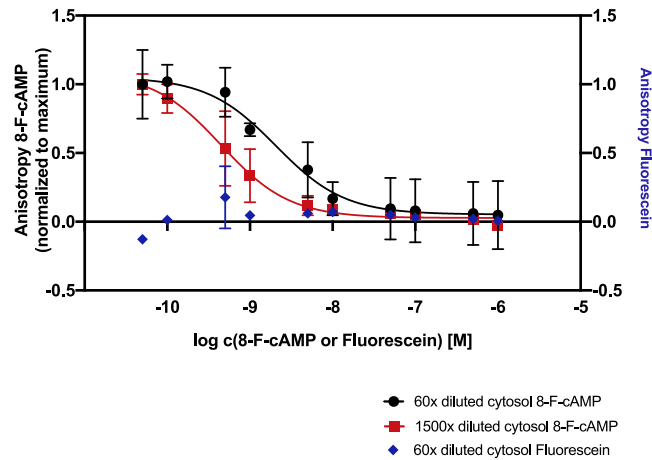


Figure S4. Quantification of the Buffering Capacity of Cytosolic Preparations Using Anisotropy, Related to Figures 2 and 7

Cytosolic preparations were prepared (STAR Methods) and diluted in binding buffer (20 mM MOPS, 150 mM NaCl, 0.005% CHAPS, 0.5 mM IBMX, pH 7) (for details on dilutions see STAR Methods). Increasing amounts of 8-F-cAMP lead to a decrease in anisotropy values, both in the 60x and 1500x diluted cytosolic preparations. The reduction in anisotropy is ascribed to the increasing ratio of free 8-F-cAMP versus bound 8-F-cAMP (at low concentrations of 8-F-cAMP, essentially all 8-F-cAMP is bound (measured by high anisotropy values) because the concentration of the dye is well below the concentration of the cAMP binding sites (i.e., the buffering capacity) in the cytosolic preparation). At increasing concentrations of 8-F-cAMP the buffering capacity of the cytosolic preparation is exceeded, and the anisotropy values decrease toward those of free 8-F-cAMP. Data are normalized to the maximal anisotropy value in order to account for the different anisotropy values observed at the two different dilutions of cytosolic preparations. Fluorescein alone does not display any binding. Solid lines connecting the mean values are meant as a guide for the eye. Data are mean \pm s.e.m. from three independent experiments.

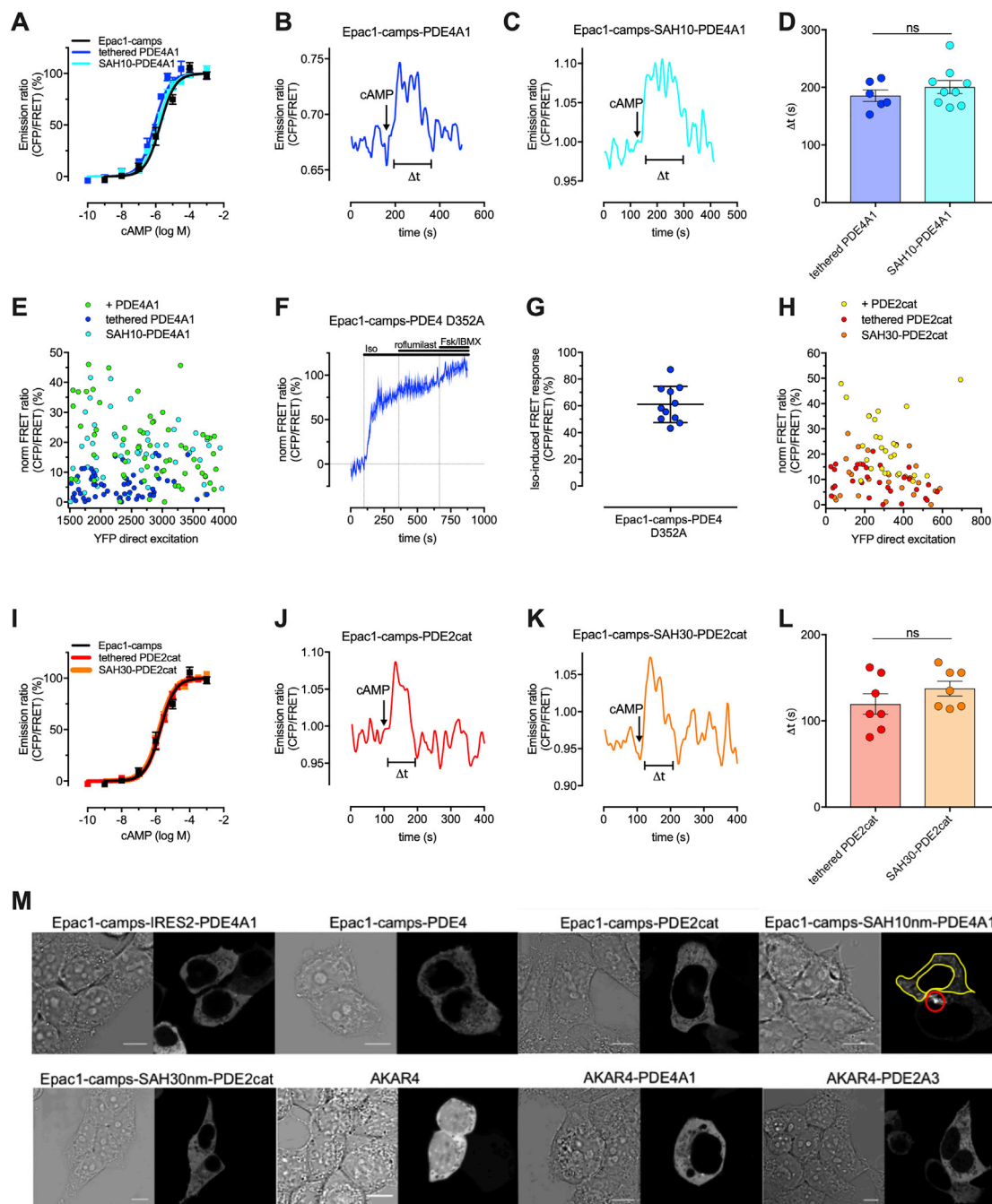


Figure S5. Affinities, Catalytic Activities, and Expression Levels of FRET Biosensors, Related to Figures 3 and 4

(A–D) PDE4A1 sensors are neither compromised in cAMP affinity nor catalytic PDE activity.

(A) Tethering PDE4A1 (blue) or SAH10-PDE4A1 (turquoise) to Epac1-camps (black) does not change the affinity of the sensor for cAMP. Shown are concentration effect curves of the normalized emission ratios (480/525 nm) obtained from cytosolic fractions of HEK293 cells expressing the indicated constructs (pre-incubated with 100 μ M IBMX) in the presence of the indicated cAMP concentrations. Data are means \pm s.e.m. of at least 3 independent experiments.

(B and C) The catalytic activity of PDE4A1 is not altered when tethered to Epac1-camps (B) or Epac1-camps-SAH10 (C). Data show one representative (out of 6–9) emission ratios (CFP/FRET) measured over time in cytosolic fractions of transfected HEK293 cells. Addition of 100 μ M cAMP (black arrow) leads to an increase in the emission ratio which is transient due to PDE4A1 activity.

(D) The ‘dwell’ times (Δt ; mean \pm s.e.m.) are a surrogate parameter for PDE activity and are not significantly different in the two constructs, according to an unpaired t test.

(E) Dependence of FRET-responses to isoproterenol on PDE4A1 expression levels. Shown are normalized FRET ratios (CFP/FRET) upon isoproterenol (10 μ M) stimulation of HEK293 cells transiently transfected with the indicated constructs, normalized to the maximum response elicited upon fsk (10 μ M)/IBMX (100 μ M)

(legend continued on next page)

stimulation. Data points show isoproterenol responses from all cells measured in [Figure 3](#). Only cells expressing the respective sensor at expression levels resulting in YFP emission values of 1500–4000 were used for the analysis. In this range, sensor expression has only a slight negative effect upon isoproterenol responses. Green: Epac1-camps + PDE4A1, blue: Epac1-camps-PDE4A1, turquoise: Epac1-camps-SAH10-PDE4A1.

(F and G) A fusion protein of Epac1-camps and a catalytically-dead PDE4A1 (D352A) senses cAMP. (F) Epac1-camps-PDE4A1 (D352A) senses cAMP increases upon Iso stimulation. Shown is an average trace from one representative coverslip (3 cells) of corrected and normalized FRET ratios in HEK293 cells transiently transfected with the indicated construct. The solid line indicates the mean, shaded areas the s.e.m. Cells were treated consecutively with isoproterenol (Iso) (10 μ M), the PDE4-inhibitor roflumilast (300 nM) and forskolin (fsk, 10 μ M)/IBMX (100 μ M). An increase in FRET, which is comparable to the experimental data of Epac1-camps (c.f. [Figure 3C](#)), was obtained directly after Iso addition. (G) Iso-induced FRET responses from experiments in (F) were normalized to FRET responses induced by fsk/IBMX (set as 100%). Data are means \pm SD from 11 cells.

(H) Dependence of FRET-responses on PDE2cat expression levels. Shown are normalized FRET ratios (CFP/FRET) upon isoproterenol stimulation of HEK293 cells transiently transfected with the indicated constructs, normalized to the maximum response elicited upon fsk (10 μ M)/IBMX (100 μ M) stimulation. Data points show isoproterenol responses from all cells measured in [Figure 4](#). Only cells expressing the respective sensor at expression levels resulting in YFP emission values of 25–800 were used for the analysis. In this range, sensor expression has only a slight negative influence upon isoproterenol responses, while FRET changes could still be robustly detected. Yellow: Epac1-camps + PDE2cat, red: Epac1-camps-PDE2cat, orange: Epac1-camps-SAH30-PDE2cat.

(I–L) PDE2cat sensors are neither compromised in cAMP affinity nor catalytic PDE activity. (I) Tethering PDE2cat (red) or SAH30-PDE2cat (orange) to Epac1-camps (black) does not change the affinity of the sensor for cAMP. Shown are concentration-effect curves of the normalized emission FRET ratios (480/525 nm) obtained from cytosolic fractions of HEK293 cells expressing the indicated constructs (pre-incubated with the PDE2-inhibitor EHNA (100 μ M) in the presence of indicated cAMP concentrations. Data are means \pm s.e.m. of at least 3 independent experiments. The catalytic activity of PDE2cat is not altered when tethered to (J) Epac1-camps or (K) Epac1-camps-SAH30. Data show one representative (out of 7) emission ratios (CFP/FRET) measured over time in cytosolic fractions of transfected HEK293 cells. Addition of 100 μ M cAMP (black arrow) leads to an increase in the emission ratio which is transient due to PDE2cat activity. (L) The 'dwell' times (Δt ; mean \pm s.e.m.) are a surrogate parameter for PDE activity and not significantly different in both constructs, according to an unpaired t test.

(M) Confocal images of all FRET-based biosensors used in this study. Indicated FRET-based biosensors were transiently expressed in HEK293 cells and fluorescence from each construct (excited using direct EYFP excitation at 514 nm) is displayed next to the Differential Interference Contrast (DIC) image. Scale bar is 10 μ m. For single-cell FRET experiments, regions of interest (ROIs) were selected taking care to analyze only regions of homogeneous expression (see example in M).

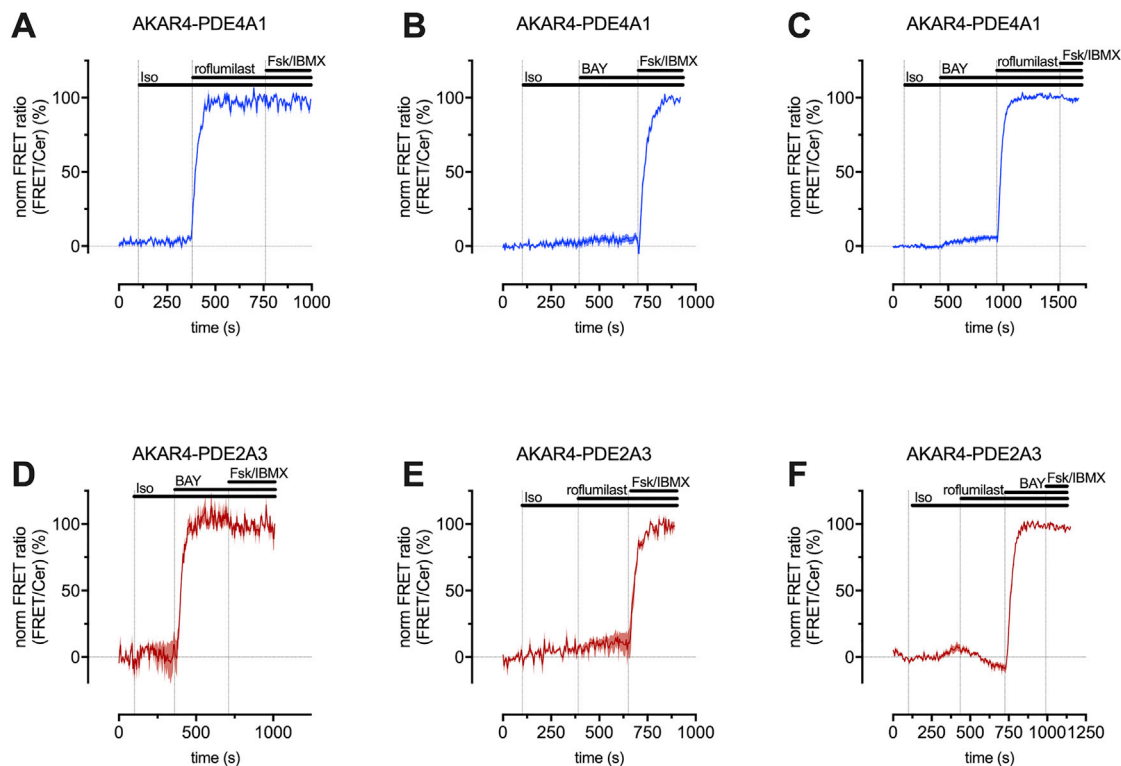


Figure S6. PDE4A1 and PDE2A3 Abolish PKA Activity Only in Their Immediate Vicinity, Related to Figure 6

(A–C) Inhibition of local PDE4A1 activity with the PDE4-inhibitor roflumilast leads to strong local PKA activity in the PDE nanodomain (A) (also cf. Figure 6) whereas treatment with the PDE2-inhibitor BAY 60-7550 has no effect (B and C).

(D–F) Inhibition of local PDE2A3 activity with the PDE2-inhibitor BAY 60-7550 leads to strong local PKA activity in the PDE nanodomain (D) (also cf. Figure 6) whereas treatment with the PDE4-inhibitor roflumilast has no effect (E, F). Shown are representative traces of normalized FRET ratios measured in HEK293 cells transiently transfected with AKAR4-PDE4A1 (A–C) and AKAR4-PDE2A3 (D and F). Cells were treated consecutively with indicated compounds (isoproterenol (Iso) (10 μ M), PDE-inhibitors (PDE4: roflumilast [300 nM], PDE2: BAY 60-7550 [100 nM]), and fsk (10 μ M)/IBMX (100 μ M)). Traces show one representative coverslip with (A) 6 cells, (B) 7 cells, (C) 5 cells, (D) 4 cells, (E) 3 cells and (F) 4 cells out of three independent experiments. Solid lines indicate the mean, shaded areas the s.e.m.

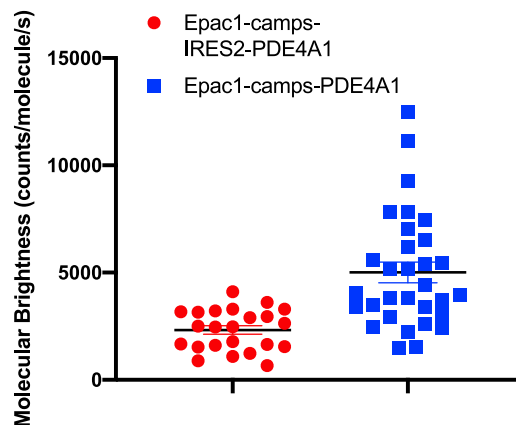


Figure S7. Characterization of the Oligomerization State of PDE4A1, Related to Figure 7

Shown are molecular brightness data of HEK293 cells transiently expressing Epac1-camps-IRES2-PDE4A1 (stoichiometric expression of Epac1-camps and PDE4A1, red circles) or Epac1-camps-PDE4A1 (tethered PDE4A1, blue rectangles). The average molecular brightness of Epac1-camps (measured by direct excitation of EYFP at 514 nm), which defines the monomeric state is 2324 photon counts/molecule/s, whereas the average molecular brightness of Epac1-camps-PDE4A1 is 5009 photons/molecule/s, indicating on average a dimer or higher order oligomers. Red circles and blue rectangles correspond to one measurement of one intact cell. Three separate transfections were investigated for each construct. Solid black lines represent the mean, error bars s.e.m.